

1-1-2005

The role of applied potentials on cracking of Zircaloy-2

Unnikrishnan Valliyil
University of Nevada, Las Vegas

Follow this and additional works at: <https://digitalscholarship.unlv.edu/rtds>

Repository Citation

Valliyil, Unnikrishnan, "The role of applied potentials on cracking of Zircaloy-2" (2005). *UNLV Retrospective Theses & Dissertations*. 1859.

<http://dx.doi.org/10.25669/rnoj-pmww>

This Thesis is protected by copyright and/or related rights. It has been brought to you by Digital Scholarship@UNLV with permission from the rights-holder(s). You are free to use this Thesis in any way that is permitted by the copyright and related rights legislation that applies to your use. For other uses you need to obtain permission from the rights-holder(s) directly, unless additional rights are indicated by a Creative Commons license in the record and/or on the work itself.

This Thesis has been accepted for inclusion in UNLV Retrospective Theses & Dissertations by an authorized administrator of Digital Scholarship@UNLV. For more information, please contact digitalscholarship@unlv.edu.

THE ROLE OF APPLIED POTENTIALS ON CRACKING OF ZIRCALOY-2

by

Unnikrishnan Valliyil

Bachelor of Engineering in Production Engineering
Bharathiar University, Coimbatore, India
April 2001

A thesis submitted in partial fulfillment
of the requirements for the

Master of Science Degree in Mechanical Engineering
Department of Mechanical Engineering
Howard R. Hughes College of Engineering

Graduate College
University of Nevada, Las Vegas
August 2005

UMI Number: 1429733

INFORMATION TO USERS

The quality of this reproduction is dependent upon the quality of the copy submitted. Broken or indistinct print, colored or poor quality illustrations and photographs, print bleed-through, substandard margins, and improper alignment can adversely affect reproduction.

In the unlikely event that the author did not send a complete manuscript and there are missing pages, these will be noted. Also, if unauthorized copyright material had to be removed, a note will indicate the deletion.

UMI[®]

UMI Microform 1429733

Copyright 2006 by ProQuest Information and Learning Company.

All rights reserved. This microform edition is protected against unauthorized copying under Title 17, United States Code.

ProQuest Information and Learning Company
300 North Zeeb Road
P.O. Box 1346
Ann Arbor, MI 48106-1346



Thesis Approval

The Graduate College
University of Nevada, Las Vegas

July 07, 2005

The Thesis prepared by

Unnikrishnan Valliyil

Entitled

The Role of Applied Potentials on Cracking of Zircaloy-2

is approved in partial fulfillment of the requirements for the degree of

Master of Science Mechanical Engineering

Examination Committee Chair

Dean of the Graduate College

Examination Committee Member

Examination Committee Member

Graduate College Faculty Representative

ABSTRACT

The Role of Applied Potentials on Cracking of Zircaloy-2

by

Unnikrishnan Valliyil

Dr. Ajit K. Roy, Examination Committee Chair
Associate Professor of Mechanical Engineering
University of Nevada, Las Vegas

Consistent with the earlier observation, this investigation revealed that Zircaloy-2 (Zr-2) may exhibit enhanced ductility at elevated temperature when tested under the combined effect of applied stress and an acidic environment. Since the cracking susceptibility of Zr-2 may be influenced by applied potentials, SCC tests were performed in a similar environment under cathodic and anodic controlled potentials (E_{cont}). While the effect of cathodic E_{cont} was insignificant, Zr-2 exhibited enhanced cracking susceptibility when tested under an anodic E_{cont} . The localized corrosion study using cyclic polarization indicates that the critical potentials became more active with increasing temperature. Secondary cracks were noted in a specimen tested under an anodic E_{cont} , as determined by optical microscopy. The primary fracture surface of the same specimen examined by scanning electron microscope (SEM) revealed combined intergranular and transgranular cracks. However, all other specimens were characterized by dimpled microstructures indicating ductile failure.

TABLE OF CONTENTS

ABSTRACT	iii
LIST OF TABLES	vi
LIST OF FIGURES	vii
ACKNOWLEDGMENTS	ix
CHAPTER 1 INTRODUCTION	1
CHAPTER 2 MATERIALS AND ENVIRONMENTS	11
2.1. Test Material	11
2.2. Test specimens	15
2.3. Test Environments	19
CHAPTER 3 EXPERIMENTAL PROCEDURES.....	21
3.1. Tensile Properties Evaluation	21
3.2. SCC Testing at Constant-load.....	23
3.3. SCC Testing Under SSR Condition.....	25
3.4. Localized Corrosion Evaluation.	30
3.5. SCC Testing Under E_{cont}	34
3.6. Optical Microcopy	35
3.7. Scanning Electron Microscopy	37
CHAPTER 4 RESULTS	39
4.1. Ambient-Temperature Tensile Testing	39
4.2. Constant-Load SCC Testing	40
4.3. Slow-Strain-Rate SCC Testing	40
4.4. Effect of Notch on s-e Diagrams in SSR Testing	44
4.5. SSR Testing Under E_{cont}	45
4.6. Localized Corrosion Study	49
4.7. Optical Microscopy.....	53
4.8. Scanning Electron Microscopy	55

CHAPTER 5 DISCUSSIONS.....	59
CHAPTER 6 SUMMARY AND CONCLUSIONS	63
CHAPTER 7 SUGGESTED FUTURE WORK	65
APPENDIX A TENSILE TESTING DATA	66
APPENDIX B SLOW-STRAIN-RATE DATA	69
APPENDIX C UNCERTAINTY AND STATISTICAL ANALYSES.....	82
BIBLIOGRAPHY.....	89
VITA.....	92

LIST OF TABLES

Table 2.1. Chemical Composition of Zr-2 (wt %)	11
Table 2.2. Ambient Temperature Mechanical Properties of Zr-2	12
Table 2.3. Physical and Mechanical properties of Zr-2	13
Table 2.4. Chemical Composition of Acidic Test Solution (gram/liter)	20
Table 2.5. Chemical Composition of Iodide Test Solution (gram/liter)	20
Table 3.1. Composition of Etchant and Applying Procedure	36
Table 4.1. Ambient Temperature Mechanical Properties	39
Table 4.2. Results of the CL SCC Tests	40
Table 4.3. Results of the SSR SCC Testing using Smooth Specimens	41
Table 4.4. Results of the SSR SCC Testing in Iodine Environment	43
Table 4.5. Results of the SSR Testing using Smooth and Notched Specimens	45
Table 4.6. Results of the SSR Testing under Cathodic E_{cont}	46
Table 4.7. Results of SSR Testing under Anodic E_{cont}	49
Table 4.8. Differences between generated and standard values	51
Table 4.9. Results of CPP testing	53

LIST OF FIGURES

Figure 1.1	Current Waste Package Design	3
Figure 1.2.	Cladding Tubes.....	4
Figure 1.3.	Breaching of Waste Package	5
Figure 1.4.	Schematic Diagram of Delayed Hydride Cracking (DHC).....	6
Figure 1.5.	Oxide-Induced Residual Stresses in SNF Cladding	8
Figure 2.1.	Allotropic Transformation of Zr-2	13
Figure 2.2.	Smooth Cylindrical Specimen.....	16
Figure 2.3.	Notched Cylindrical Specimen.....	16
Figure 2.4.	Geometric Stress Concentration Factor for Notched Specimen.....	17
Figure 2.5.	Configuration of Spot-Welded Cylindrical Specimen	18
Figure 2.6.	Electrochemical Polarization Specimen.....	19
Figure 3.1.	MTS Test Setup.....	23
Figure 3.2.	Typical Calibration Curve of a Proof Ring	24
Figure 3.3.	Constant-load Test Setup.....	25
Figure 3.4.	Slow-Strain-Rate Test Setup	26
Figure 3.5.	SSR Test Setup with Accessories.....	28
Figure 3.6.	Load Frame Compliance Test Results.....	28
Figure 3.7.	CPP Diagram for an Active-Passive Material	32
Figure 3.8.	Luggin Probe Arrangement	33
Figure 3.9.	CPP Test Setup.....	34
Figure 3.10.	SCC Test Setup under Controlled Potential	35
Figure 3.11	LEICA Optical Microscope.....	37
Figure 3.12.	JEOL-5600 Scanning Electron Microscope	38
Figure 4.1.	Stress versus Strain Diagrams for Smooth Specimens in Acidic Environment.....	41
Figure 4.2.	Stress versus Strain Diagrams for Smooth Specimens in Iodine Environment.....	43
Figure 4.3.	Comparison of Smooth and Notched Specimens Tested under SSR Condition.....	44
Figure 4.4.	Stress-Strain Diagrams for Zr-2 under Cathodic E_{cont}	46
Figure 4.5.	E_{cont} Vs Ductility Parameters in SSR Testing.....	47
Figure 4.6.	Stress-Strain Diagrams for Notched Specimens under Cathodic E_{cont}	48
Figure 4.7.	Stress-Strain Diagrams under Anodic E_{cont}	49
Figure 4.8.	Standard ASTM G 5 Potentiodynamic Polarization Curve	50
Figure 4.9.	Generated ASTM G 5 Potentiodynamic Polarization Curve	51
Figure 4.10.	CPP Diagram of Zr-2 at 30°C.....	52
Figure 4.11.	CPP Diagram of Zr-2 at 90°C.....	52
Figure 4.12.	Effect of Temperature on Critical Potentials.....	53
Figure 4.13.	Optical Micrograph of Zr-2, HF+HNO ₃ +H ₂ O, 100X.....	54

Figure 4.14. Optical Micrograph of Zr-2 Showing Secondary Cracks	54
Figure 4.15. Figure 4.15. SEM Micrographs of Test Specimens, 150 X	55
Figure 4.16. SEM Micrographs of Zr-2, 90°C Acidic Iodine Solution, 150 X	56
Figure 4.17. SEM Micrographs of Zr-2 under Cathodic Potentials, RT Acidic Solution, 150 X	57
Figure 4.18. SEM Micrograph of Zr-2 under Anodic Potential, RT Acidic Solution, 150 X	58

ACKNOWLEDGMENTS

This work was performed under the able guidance of my advisor, Dr. Ajit K. Roy. It was my privilege and pleasure to work with him on this project and I would like to express my gratitude to him for his invaluable contributions in this investigation.

I would like to thank Dr. Anthony E. Hechanova, Dr. Woosoon Yim and Dr. Edward S. Neumann, for their valuable suggestions and support throughout this study.

I would like to acknowledge the assistance offered by my associates in the Materials Performance Laboratory.

CHAPTER 1

INTRODUCTION

Spent nuclear fuel (SNF) and high-level radioactive waste (HLW) are the result of commercial power generation, nuclear weapons production, and other research activities. The disposal of SNF from operating nuclear plants and other research and development activities poses a severe challenge to scientists all over the world. This is due to the fact that radioactive waste can create potential hazards, and requires safe and environmentally-acceptable forms of disposal. Scientists and engineers have studied different ways to dispose of these highly radioactive materials. Currently, these radioactive wastes are being stored at government facilities or at the nuclear power plants where they are generated. There are two acceptable methods for storing SNF at the reactor site. One method is to store them in specially-designed pools at the individual reactor site. Once the pool capacity is reached, the SNF/HLW can be stored in casks located above ground. ⁽¹⁾ This storage method is called the dry cask storage. Dry cask storage allows spent fuel that has already been cooled in the spent fuel pool for at least one year to be surrounded by inert gas inside a container called a cask. The casks are typically steel cylinders that are either welded or bolted closed. The steel cylinder provides a leak-tight containment of the spent fuel. Each cylinder is surrounded by additional steel, concrete, or other material to provide radiation shielding to workers and members of the public. These storage methods can at best be described as temporary.

Studies indicate that the total inventory of SNF and HLW in the U.S. could exceed 70,000 metric tons of heavy metal (MTHM) by the end of 2010. ⁽²⁾ Thus, a permanent disposal site is needed as these wastes are being accumulated year after year. Most researchers around the world believe that the viable location to emplace these radioactive wastes would be a geologic repository. According to the standards prescribed by United States Environmental Protection Agency (EPA), a repository may not pose any greater risk than the unmined uranium from which the nuclear fuels are produced. However, strict regulations must be maintained for prevention of the release of radioactive species while the nuclear wastes are emplaced in the repository. During the disposal period, the radioactivity of SNF will naturally decrease or decay. According to the EPA standards, the SNF may no longer pose threats to public health and safety after 10,000 years of radioactive decay. ⁽³⁾

The Yucca Mountain site near Las Vegas, Nevada has recently been proposed to be the nation's geologic repository to contain SNF/HLW. This location was identified to be the most desired site due to a variety of reasons inclusive of the dry climate (combined average precipitation of 7.5 inches per year) and the deep water table (800 to 1,000 feet below the level of the potential repository). These requirements are necessary for a geologic repository since the ground water may become contaminated due to the release of radionuclides from SNF during their storage. Even though the Yucca Mountain site has the natural barriers to prevent the seepage of water into the waste package, other engineering designs were also considered to prevent water contact with the waste package.

The current waste package design is based on an all-metallic multi-barrier concept to accommodate the geologic disposal of SNF/HLW. This design includes a titanium (Ti) drip shield, an outer barrier made of a nickel-base alloy (Alloy-22), and an inner container made of austenitic Type 316NG stainless steel, as shown in Figure 1.1. The Ti Grade-7 is highly corrosion resistant, with general corrosion penetrating only about 0.08 inches in 10,000 years. This drip shield may protect the waste package against rockfall and dripping water. The Alloy-22 outer barrier could provide the required corrosion protection, while the Type 316NG stainless steel may provide the necessary structural support. The general corrosion rate of Alloy-22 could be as low as 0.03 inches after a disposal period of 10,000 years. ⁽⁴⁾

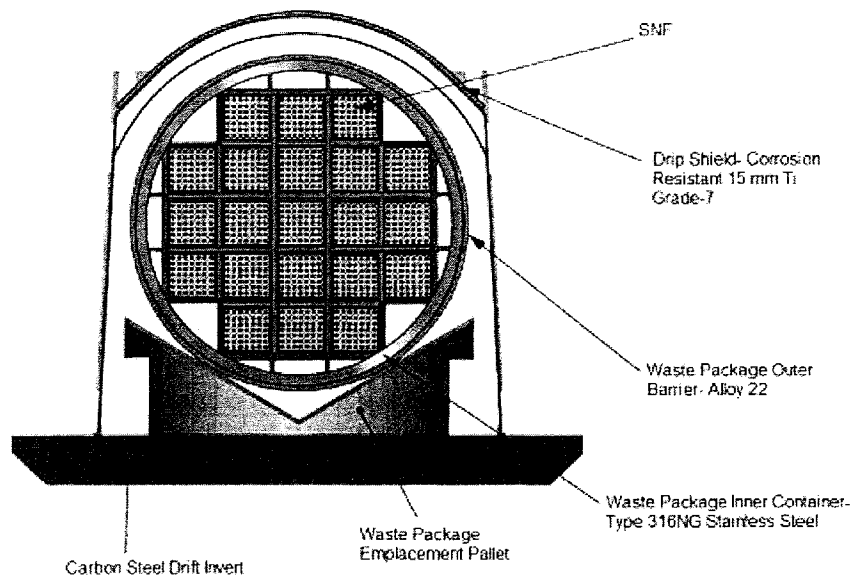


Figure 1.1. Current Waste Package Design

The SNF is usually contained as pellets inside the cladding tubes, as illustrated in Figure 1.2. Cladding is the primary structural barrier that prevents the release of radionuclides. The SNF cladding is made of zirconium (Zr) alloy such as zircaloy-2 (Zr-2), which is very corrosion-resistant. Zr alloys are generally used due to their low neutron capture cross-section, excellent corrosion resistance and desirable mechanical properties at both ambient and elevated temperatures.⁽⁵⁾ During the prolonged storage of SNF/HLW, the engineered barrier systems may experience a reduction in their structural integrity, and the water from the surrounding environment could come in contact with the nuclear waste, thus, dissolving it, and carrying some of the radionuclides into the underlying rocks. Thus, the structural integrity of the SNF cladding material plays an important role in either preventing or minimizing the release of these radionuclides.

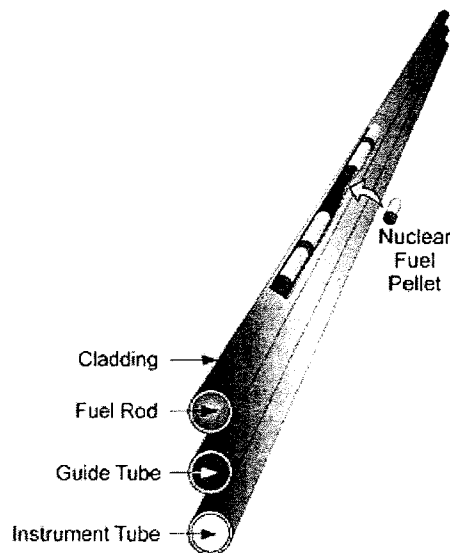


Figure 1.2. Cladding Tubes

Significant studies have been performed in the past ⁽⁶⁾ to evaluate the suitability of Zr and its alloys for nuclear-related applications. Pure Zr and its alloys are highly corrosion-resistant due to their capability to form protective oxide layers on their surfaces. However, they may become susceptible to stress-corrosion-cracking (SCC), hydrogen-embrittlement (HE), and localized (pitting and crevice) corrosion if the waste package containers become breached by the surrounding aqueous environments. A possible scenario for breaching is illustrated in Figure 1.3. Breaching may occur due to a combination of factors including the type of the container materials, their surface conditions, residual stresses generated due to fabrication, and irradiation products.

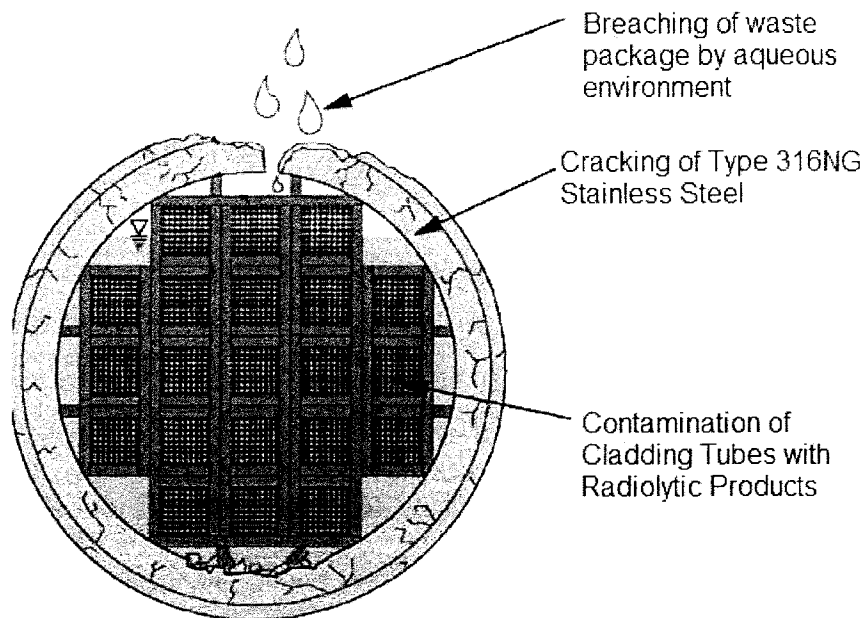


Figure 1.3. Breaching of Waste Package

The presence of impurities and alloying elements in the waste package container materials can play a significant role in influencing the corrosion behavior of Zr alloys.

Internal stresses induced in the Zr alloys due to plastic deformation and welding, and their interaction with the irradiation products can lead to embrittlement including SCC/HE. The breaching of the waste package by moisture and aqueous phases can lead to the radiolysis of water, producing a variety of products such as hydrogen peroxide (H₂O₂) and nitric acid (HNO₃).⁽¹⁾ Eventually, atomic and molecular hydrogen can be formed from these products, which along with the residual stresses can lead to the occurrence of SCC and HE in the Zr alloys.

Delayed-hydride-cracking (DHC) is another form of environment-induced degradation that may occur in Zr and its alloys. DHC is a sub-critical crack growth phenomenon occurring in Zr alloys as well as other hydride-forming materials that requires the formation of brittle hydride phases at the tip of a crack with its subsequent failure, resulting in crack extension⁽⁷⁾ as illustrated in Figure 1.4. In order to initiate DHC in Zr alloys, hydrogen and a stress gradient must be present to promote the diffusion process. Hydrogen can be formed by the radiolysis of water as well as the reaction of Zr alloys with water, as shown below.

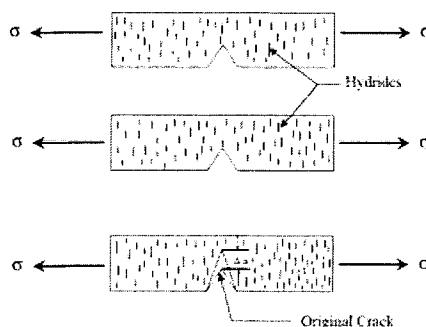
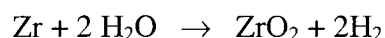


Figure 1.4. Schematic Diagram of Delayed Hydride Cracking (DHC)

The hydrogen produced by the above reaction can combine with Zr to form zirconium-hydride ($\text{ZrH}_{1.5}$) platelets when a critical solubility limit is reached. These $\text{ZrH}_{1.5}$ platelets can then precipitate along some preferred orientation in areas near a stress gradient developed by residual stresses. The plane, normal to the hydride platelet, is usually parallel to the tensile axis. Since the hydrides are more brittle than the metal matrix, they tend to undergo fracture under the effect of stress at the crack tip. The primary crack then rapidly propagates through the embrittled region until the crack front is finally arrested at the end of the hydrided region by the ductile Zr matrix. A new hydrided zone is eventually formed at the crack tip. This process repeats itself, and the crack propagates in a step-wise manner.

The metallic layer of the cladding, which is in contact with the thick outer oxide layer, may be subjected to a large amount of compressive stresses. ⁽⁸⁾ These stresses can primarily be generated as a result of large expansion in volume of the Zr-oxide (ZrO_2), as shown in Figure 1.5. The stress intensity with a flaw, located in the metallic layer which is in contact with the outer oxide layer, is a strong function of the thickness of the adherent uncracked oxide layers. The metallic layer, in contact with the oxide layer usually contains high-density circumferential hydrides, whereas the hydride density in the metallic layer in contact with the fuel pellets is relatively lower.

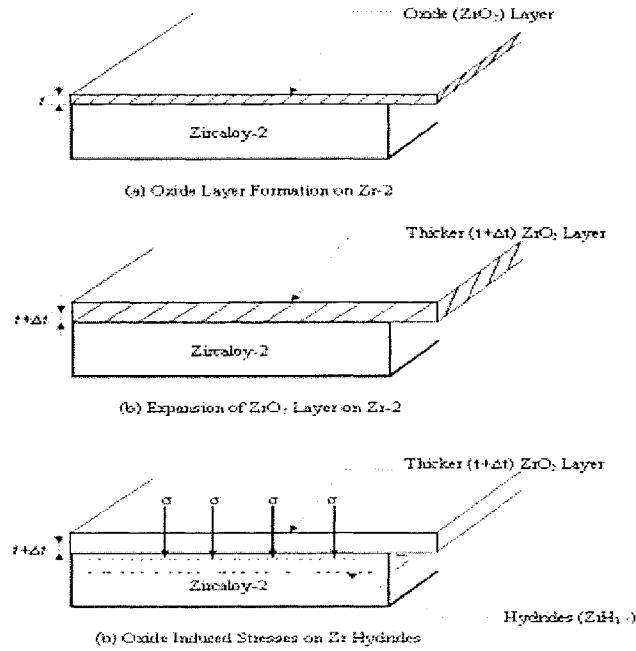


Figure 1.5. Oxide-Induced Residual Stresses in SNF Cladding

The initiation of DHC in the metallic region located in the inner diameter side i.e. on the pellet side is least concerned under the repository conditions due to the relatively higher temperature and lower stress, thus resulting in lower stress intensity, reduced potential for hydrogen diffusion, hydride reorientation and hydride blistering. The fundamental process of DHC initiation under this scenario consists of nucleation, growth, and cracking of hydride blisters in the outer diameter side of the metallic region, especially in the vicinity of some localized hydrogen accumulation spots.⁽⁹⁾

There are indications in the literature⁽¹⁰⁾ that Ni in Zr-2 may be responsible for hydrogen pickup. This observation has led to the development of a Zr alloy known as zircaloy- 4 (Zr-4), which does not contain Ni. Zr-4 has been known to be less susceptible

to hydrogen-induced-cracking (HIC). The addition of Nb to Zr-4 can further reduce the amount of hydrogen absorption.

The embrittlement of engineering metals and alloys in the presence of aqueous environments can also occur under the influence of both anodic and cathodic potentials. There are indications in the open literature ⁽¹¹⁾ that an anodic shift in the electrochemical potential may occur in metals and alloys inside a repository due to the irradiated aqueous environments. This anodic shift can cause the potential to lie in a region where localized corrosion such as pitting and anodic dissolution may occur. The anodic dissolution process involves the breakdown of surface film at a localized region due to the interaction of aggressive chemical species such as chloride ion (Cl^-) with the metal surface. The application of tensile stress can further enhance the cracking susceptibility of a material by accelerating the cracking tendency at the localized region.

From an electrochemical point of view, active-passive materials such as Zr alloys can undergo breakdown of surface film at or above the critical pitting potential (E_{pit}) due to the increase in current density. It has been reported ⁽¹²⁾ that Zr and its alloys can undergo cracking in the presence of aggressive species at applied potentials more noble to the E_{pit} value while the material is loaded in tension.

This investigation is focused on the evaluation of the cracking susceptibility of Zr-2 in an environment relevant to the proposed geologic repository at the Yucca Mountain site. Since Zr alloys have been cited ⁽¹²⁾ to undergo enhanced degradation in aqueous environments under either an anodic or a cathodic applied potential, efforts have been made in this investigation to study the cracking phenomenon of Zr-2 under both anodic

and cathodic controlled potentials (E_{cont}). The susceptibility of Zr-2 to localized corrosion has also been determined by an electrochemical polarization technique.

The cracking susceptibility of Zr-2 has been studied under two different types of loading conditions, namely constant-load (CL) and slow-strain-rate (SSR). In many instances, the cracking susceptibility of a material cannot be determined in short term tests at a constant load even in the presence of very hostile environments. Thus, the SSR technique has the merit of ensuring failure in an environment of interest due to the combined effect of an applied stress at an optimum strain rate and a potent environment. Indeed, the application of an external potential is expected to influence the cracking tendency to some extent.

The SSR technique was also used due to its simplicity in testing and short duration needed to achieve conclusive test results. The parameters used in this type of testing to characterize the cracking tendency include the percent elongation (%El), the percent reduction in area (%RA) and the metallurgical parameters such as the time-to-failure (TTF), the true failure stress (σ_f) and the failure strain (ϵ_f). The magnitude of E_{cont} was based on either the open-circuit-potential / corrosion-potential (E_{corr}), or the critical-pitting-potential (E_{pit}) determined by the polarization experiments in a similar environment. The metallurgical microstructures, and the extent and morphology of degradation of Zr-2 were analyzed by optical microscopy and scanning electron microscopy (SEM), respectively. The experimental details including the materials, environment, testing techniques and the analyses of the resultant data are presented in the next few sections of this thesis.

CHAPTER 2

MATERIAL AND ENVIRONMENTS

2.1. Test Material

The material tested in this investigation was Zircaloy-2 (Zr-2), which is a commercially available cladding material for nuclear applications.^(13, 14) This alloy contains predominantly (98%) elemental zirconium and very low alloy content, as given in Table 2.1.

Table 2.1. Chemical Composition of Zr-2 (wt %)⁽¹⁵⁾

Material/Heat No	Cr	Fe	Ni	Fe+Cr+Ni	O	Sn	Zr
Zr-2/242831	0.10	0.182	0.070	0.352	0.127	1.298	Balance

Zr-2 possesses many desirable properties including reasonable high tensile and creep strength, enhanced ductility following irradiation and excellent corrosion resistance. Further, the low absorption cross section for neutrons makes this alloy a suitable material for application as a cladding fuel element in nuclear reactors.⁽¹⁶⁾ This material is generally used in a solution- annealed condition. The typical tensile properties of Zr-2 in a solution-annealed condition at ambient temperature are shown in Table 2.2.

Table 2.2. Ambient Temperature Mechanical Properties of Zr-2 ⁽¹⁷⁾

Material/ Heat No	Yield Strength, ksi, (Mpa)	Ultimate Tensile Strength, ksi, (Mpa)	%EI	%RA
Zr-2/242831	53.25 (367.16)	78.7 (542.64)	27.5	NA

It has been suggested ⁽¹⁸⁾ that the cladding materials for SNF should have high melting temperature to withstand abnormal operating conditions such as high temperature transients. Further, the thermal conductivity of these alloys should be sufficiently high to minimize thermal stresses resulting from the temperature differences associated with the conventional nuclear reactor operating conditions. All these requirements can easily be met by Zr-2 in view of its high melting point, adequate strength, good thermal conductivity, low thermal expansion, good transparency to thermal neutrons and excellent corrosion resistance.

The excellent corrosion resistance of zirconium alloys such as Zr-2 can be attributed to the formation and growth of a protective oxide film on its surface. This film is very adherent, self healing, and protects the substrate from chemical and mechanical damage at temperatures up to 300 °C. The presence of these protective oxide films on the surface of Zr-2 can prevent corrosion damage in many environments including most mineral and organic acids, strong alkalis, saline solutions and some molten salts. ⁽¹⁴⁾ Corrosion attack can also be resisted by Zr-2 in oxidizing media in the absence of halides.

Zirconium alloys usually have a hexagonal close packed (hcp) crystal structure. However, they can undergo allotropic transformation at a temperature of 870°C (1590 °F)

when the crystal structure can change from hcp to body centered cubic (bcc) as shown in Figure 2.1.

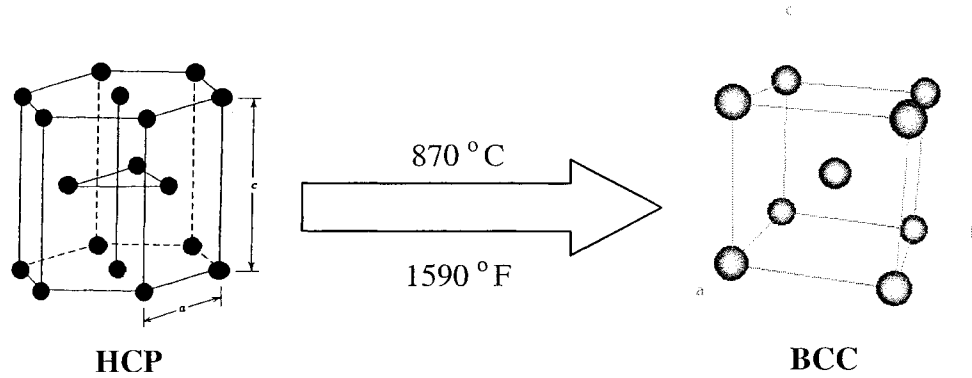


Figure 2.1. Allotropic Transformation of Zr-2

The presence of elements such as Tin (Sn), Nitrogen (N) and Oxygen (O) can raise this transformation temperature. On the other hand, elements such as Iron (Fe), Chromium (Cr) and Nickel (Ni) can lower this transition temperature, thus showing an opposite effect. The typical physical and mechanical properties of Zr-2 are shown in Table 2.3.

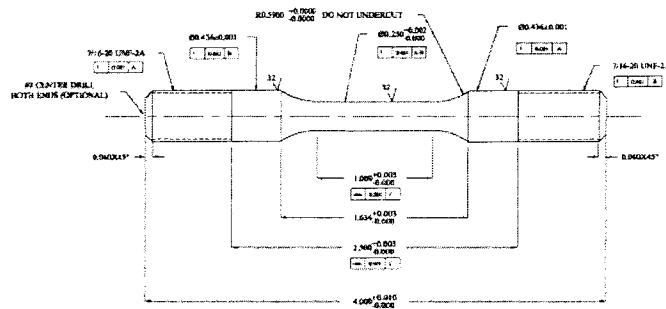
Table 2.3. Physical and Mechanical properties of Zr-2 ⁽¹⁹⁾

Physical Properties	
Density at 20 °C (70 °F), g/cm ³	6.56
Crystal Structure	
α-phase	hcp (<865 °C or 1590 °F)
β-phase	bcc (>865 °C or 1590 °F)
(α+β) phase	---
Melting Point, °C (°F)	1850 (3362)
Boiling Point, °C (°F)	4375 (7907)
Coefficient of Thermal Expansion per °C (°F)×10 ⁻⁶ at 25 °C (75 °F)	6.0 (10.8)
Thermal Conductivity at 300-800 K, W/m*K (Btu*ft/h*ft ² *°F)	21.5 (12.7)
Specific Heat, J/kg*K (cal _m /g*K)	285 (0.068)
Electrical Resistivity, μΩ*cm at 20 °C (70 °F)	74.0
Mechanical Properties	
Modulus of Elasticity, GPa (10 ⁶ psi)	99.3 (14.4)
Shear Modulus, GPa (10 ⁶ psi)	36.2 (5.25)
Poisson's Ratio at Ambient Temperature	0.37

2.2. Test specimens

Smooth and notched cylindrical specimens having 4-inch overall length (101.6 mm), 1-inch gage length (25.4 mm) and 0.25-inch gage diameter (6.35 mm) were machined by a qualified vendor using the annealed bar stocks. These specimens were machined in such a way that the gage section was parallel to the longitudinal rolling direction. The gage length (l) to the diameter (d) ratio (l/d) of both smooth and notched specimens was maintained at 4 according to the ASTM designation E 08.⁽²⁰⁾ The notched cylindrical specimens had a circular notch of diameter 0.156-inch (3.96 mm) with a root radius of 0.047-inch (1.194 mm) at the centre of the gage section.

The notched specimens were tested to study the effect of stress concentration on both the tensile properties and the SCC susceptibility determined by CL and SSR testing techniques. The magnitude of stress concentration factor (k_t) was 1.45, as determined by the calculations shown below and Figure 2.4. The dimensions and the pictorial view of the smooth and notched cylindrical specimens are shown in Figures 2.2 and 2.3 respectively.

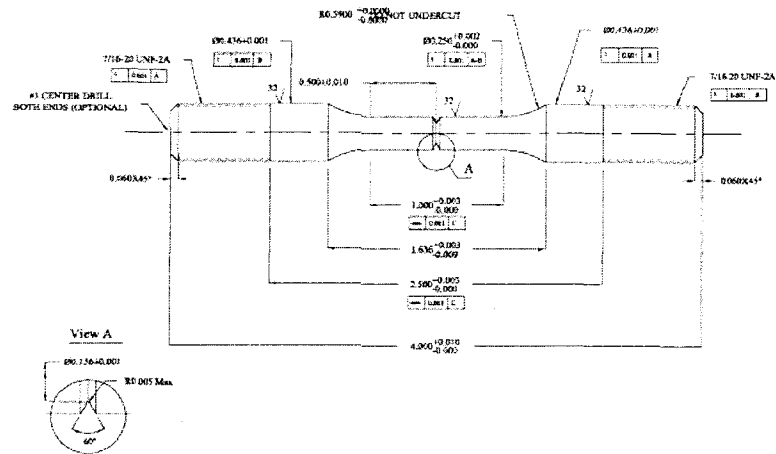


(a) Dimensions of Smooth Cylindrical Specimen



(b) Configuration of Smooth Cylindrical Specimen

Figure 2.2. Smooth Cylindrical Specimen



(a) Dimensions of Notched Cylindrical Specimen



(b) Configuration of Notched Cylindrical Specimen

Figure 2.3. Notched Cylindrical Specimen

The ratios of D/d and r/d were used to estimate the magnitude of the stress concentration factor (k_t)^[21] on the following analysis and the theoretical value of stress concentration factor (k_t) was determined as 1.45.

$$\frac{D}{d} = \frac{0.250in}{0.156in} = 1.60$$

$$\frac{r}{d} = \frac{0.047}{0.156} = 0.30$$

Where,

D = Gage diameter of the specimen

d = Notch diameter of the specimen

r = Radius of curvature at the root of the notch

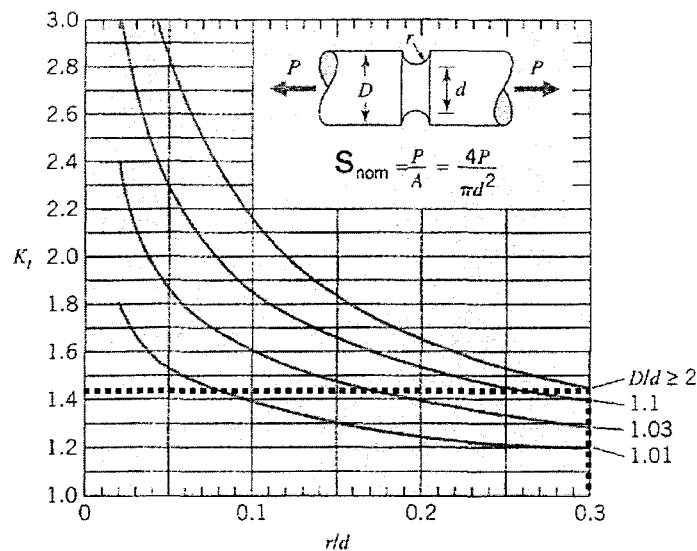


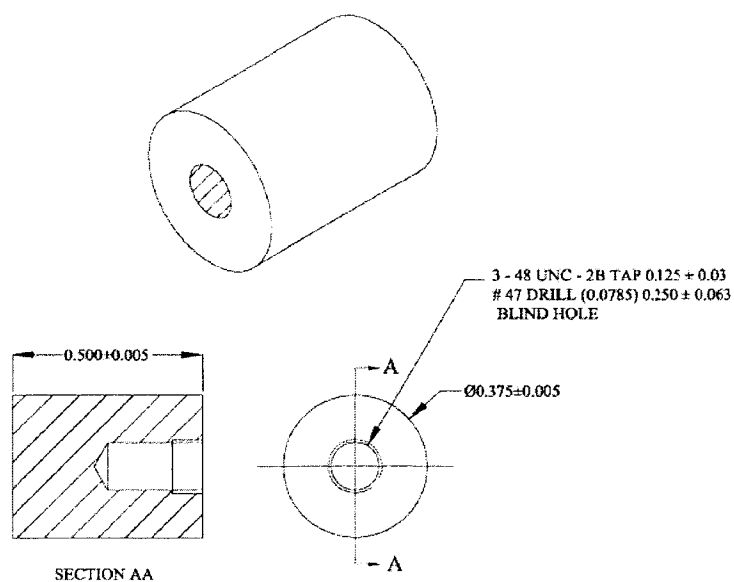
Figure 2.4. Geometric Stress Concentration Factor for Notched Specimen⁽²¹⁾

The cylindrical specimens used in the E_{cont} testing were spot welded with a conductive wire to polarize them either anodically or cathodically. The conductive wire was coated with lacquer to prevent its direct contact with the test solution during polarization. The configuration of the spot-welded cylindrical specimen is shown in Figure 2.5.



Figure 2.5. Configuration of Spot-Welded Cylindrical Specimen

Cylindrical specimens having length and diameter of 0.50-inch (12.7 mm) and 0.37-inch (9.398 mm), respectively, with a central blind hole parallel to the cylindrical axis was used in electrochemical polarization experiments to evaluate the localized corrosion behavior according to the ASTM Designation G 5.⁽²²⁾ The dimensions and pictorial view of the polarization specimens are shown in Figure 2.6. Since the localized corrosion susceptibility of a material of interest can be a function of the surface finish, the polarization specimens were polished with a 600 grid paper prior to the testing.



(a) Dimensions of Polarization Specimen



(b) Configuration of Polarization specimen

Figure 2.6. Electrochemical Polarization Specimen

2.3. Test Environments

Previous studies performed on zirconium alloys at UNLV^(23, 24) have demonstrated that these alloys may not undergo any cracking either in a neutral or an acidic solution irrespective of the testing techniques used. Since no cracks were observed in the previous investigations, SCC tests were performed in the current study only in an acidic solution, with and without controlled electrochemical potentials. The selection of an acidic environment was based on the aggressiveness of the testing solution in terms of

its pH value (~ 2). The chemical composition of the acidic solution used in this investigation is similar to that of the previous investigation ^(23, 24) and is shown in Table 2.4.

Table 2.4. Chemical Composition of Acidic Test Solution (gram/liter)

Environment	CaCl ₂	K ₂ SO ₄	MgSO ₄	NaCl	NaNO ₃	Na ₂ SO ₄	HCl
Acidic Solution	2.77	7.58	4.95	39.97	31.53	56.74	To achieve the desired pH value

It has been reported ⁽¹²⁾ that zirconium alloys may undergo cracking in an aqueous solution containing iodine. Therefore, a limited number of SCC testing was also performed in an acidic environment containing sodium iodide. The composition of this test solution is given in Table 2.5.

Table 2.5. Chemical Composition of Iodide Test Solution (gram/liter)

Solution (pH)	NaI	H ₂ SO ₄
Iodide (1.0)	10.0	Added to adjust the desired pH

CHAPTER 3

EXPERIMENTAL PROCEDURES

As the title of this thesis implies, this investigation is primarily focused on the evaluation of the cracking susceptibility of Zircaloy-2 (Zr-2) in an acidic environment, with and without the application of an external controlled potential (E_{cont}). Both anodic and cathodic potentials have been applied to the test specimens to evaluate their susceptibility to stress corrosion cracking (SCC) under E_{cont} . The SCC susceptibility has been determined under constant-load (CL) and slow-strain-rate (SSR) testing conditions. The ambient temperature tensile properties of Zr-2 were determined by a conventional mechanical testing equipment. The localized corrosion (pitting and crevice) susceptibility was determined by the cyclic potentiodynamic polarization (CPP) technique. The metallographic and fractographic evaluations of the tested specimens were performed by optical microscopy and scanning electron microscopy (SEM), respectively. The detailed experimental techniques are described in the following subsections.

3.1. Tensile Properties Evaluation

The tensile properties including the ultimate tensile strength (UTS), the yield strength (YS) and the ductility parameters such as the percentage elongation (%El) and the percentage reduction in area (%RA) of Zr-2 were evaluated at ambient temperature using

an axial/torsional servohydraulic MTS machine. The smooth and notched cylindrical specimens were pulled at a strain rate of 10^{-3} /sec according to the ASTM Designation E 08-04.⁽²⁰⁾ A minimum of two specimens were tested under each experimental condition, and the average value was reached. The load, time, and extensometer reading were recorded in the data file at the rate of 100 data points/sec. The engineering stress versus engineering strain diagrams were developed using these data. The magnitude of the YS was determined by the point of intersection of a line drawn parallel to the linear portion of this curve at a strain offset value of 0.2%. UTS, %El and %RA were also determined from these plots as well as the dimensions of the cylindrical tensile specimen before and after testing.

The MTS unit model 319.25, shown in Figure 3.1, had an axial load transducer of 55 kip (250 kN) and a torsional load transducer of 20,000 lbf-in (2200 N-m) capacity. It had a hydraulically-controlled actuator with 5.5" stroke and approximately 55° angular rotation. It consisted of a large heavy-duty load frame with an adjustable crosshead attached to the wedge grip at the top, and a movable actuator with another wedge grip at the bottom to enable loading and unloading of the test specimen. The axial motion was controlled by force, displacement, or an external signal from the strain gage. The torsional motion was controlled by torque, angular position, or an external signal from the strain gage. The specimen was mounted between two wedge grips and was pulled by the movable actuator. The load cell, contained in the crosshead, measured the applied force on the tensile specimen. The movement of the crosshead, relative to the locked crosshead, generated the strain within the specimen and consequently, the corresponding load.

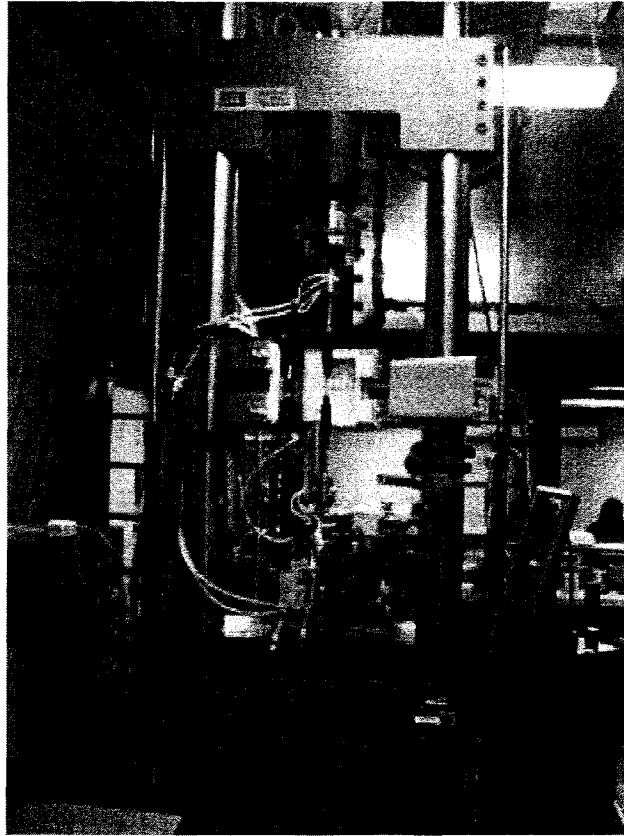


Figure 3.1. MTS Test Setup

3.2. SCC Testing at Constant-load.

For constant-load (CL) testing, calibrated proof rings were used. Proof rings were specifically-designed to meet the National Association of Corrosion Engineers (NACE) standard TM-01-77.⁽²⁵⁾ Each individually calibrated proof ring was made by Cortest Inc, and was accompanied by a calibration curve showing the load versus deflection of this ring. The test specimens were loaded under a stress state of uniaxial tension. The ring deflection was measured by a 8-9" micrometer, with the supplied dial indicator providing a check. These poof rings were fabricated from precision-machined alloy steel. The

tension on the proof ring was quickly and easily adjusted using a standard wrench on the tension-adjusting screw and lock nut. A thrust bearing distributed the load and prevented seizure. The specimen grips in these proof rings were made of stainless steel to be fully-resistant to the testing environment. The environmental test chamber was secured by O-ring seals that fully prevented any leakage during testing. These chambers made of Hastelloy C-276, were designed for test conditions ranging from ambient temperature and pressure to 220°C and pressure exceeding 2,000 psi, respectively.

The amount of deflection needed to apply the desired load in CL testing was determined by use of the calibration curve of the proof ring, as shown in Figure 3.2. The magnitude of the applied stress was based on the ambient temperature tensile yield strength (YS) of the test materials. The specimens were loaded at stress values equivalent to different percentages of the material's YS value, and the corresponding time-to-failure (TTF) was recorded. The determination of the SCC tendency using this technique was based on the TTF for the maximum test duration of 30 days. An automatic timer attached to the test specimen recorded the TTF.

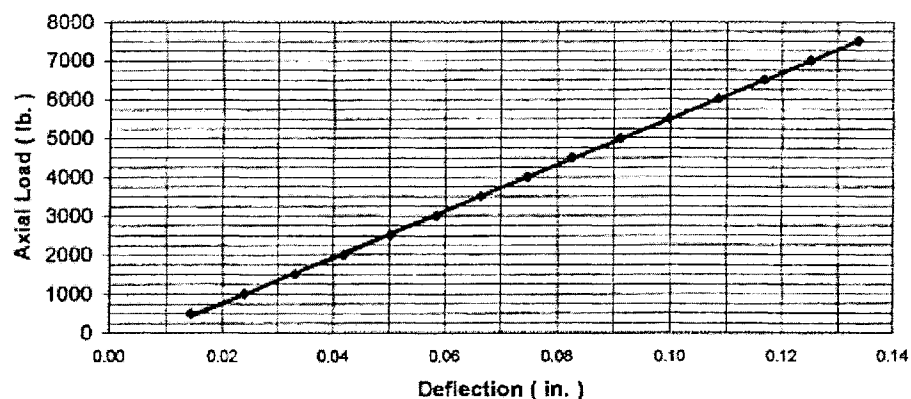


Figure 3.2. Typical Calibration Curve of a Proof Ring

For this type of testing, the cracking susceptibility was generally expressed in terms of a threshold stress (σ_{th}) below which cracking did not occur during the maximum test duration of 30 days. ⁽²⁶⁾ The experimental setup used in CL Testing is shown in Figure 3.3.

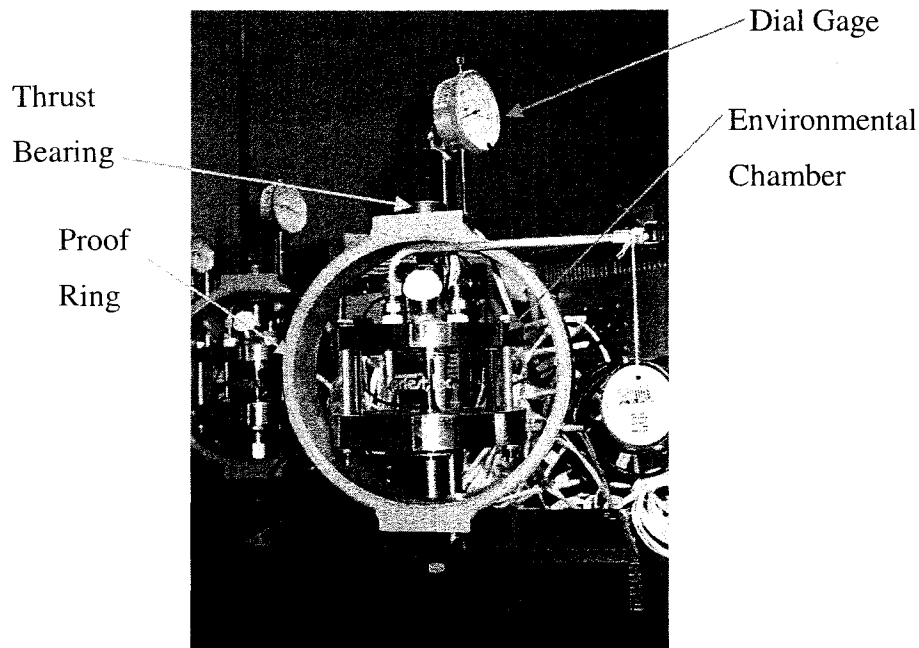


Figure 3.3. Constant-load Test Setup

3.3. SCC Testing Under SSR Condition

The SSR testing, also known as the constant extension rate testing (CERT), is a dynamic SCC evaluation technique. The SSR testing setup used in this investigation is shown in Figure 3.4. During SSR testing, the specimen was continuously strained in tension until fracture, according to the ASTM Designation G 129 ⁽²⁷⁾, in contrast to more conventional SCC testing conducted under a sustained loading condition. The application of a dynamic plastic strain reduces the initiation time for the onset of cracking and cause

an accelerated rupture of the surface films of the test material. This type of testing can cause failure in a material that probably might not occur under a CL condition or might have taken a prohibitively longer duration to initiate cracks in producing failures in it. ⁽²⁸⁾

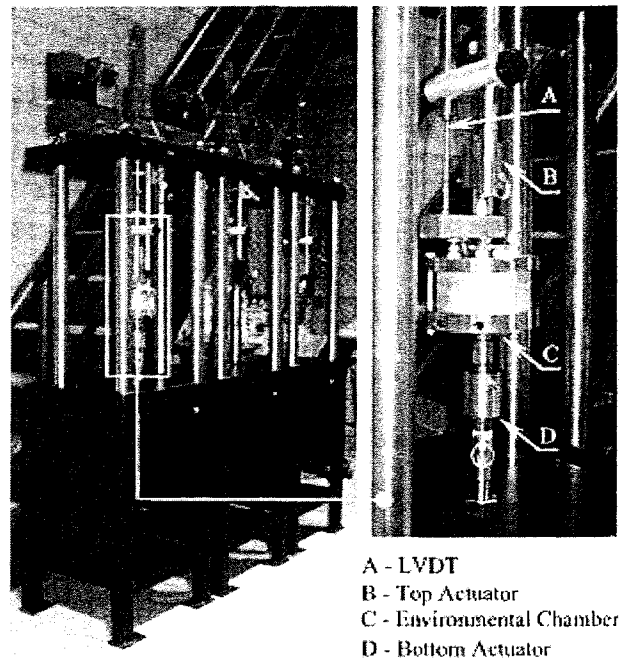


Figure 3.4. Slow-Strain-Rate Test Setup

The primary advantage of the SSR testing technique is that it allows the evaluation of the effects of metallurgical variables such as alloy composition, heat-treatment, microstructure, and environmental parameters in a relatively short duration. The SSR testing unit employed in this study had a load capacity of 7500 pounds with linear extension rates ranging from 10^{-5} to 10^{-8} in/sec. This unit contained a heavy-duty load-frame to minimize the system compliance but at the same time maintained the precise

axial alignment of the load train. An all-gear drive system provided the consistent extension rate.

The SSR test setup used in this investigation consisted of a top-loaded actuator, testing chamber, linear variable differential transducer (LVDT), load cell, specimen grips, stepper motor, motion controller, thermocouple, heating coil, temperature controller and accessory support, as shown in Figure 3.5. The top-loaded actuator was intended to pull the specimen at a specified strain rate, so that the spilled solution, if any, would not damage the actuator. A heating coil was connected to the bottom cover of the environmental chamber for elevated-temperature testing. A thermocouple was connected through the top cover of this chamber to monitor the testing temperature. The load cell was intended to measure load through an interface with the front panel. The LVDT was used to record the displacement of the gage section during straining.

Prior to the SCC testing, the load-frame-compliance factor (LFCF), which is defined as the deflection in the frame per unit load, was determined by using an all-thread ferritic Type 430 stainless steel specimen. This test is used to compensate for the stretch in the load frame components. The generated LFCF data are shown in Figure 3.6. The LFCF values were fed to the load frame acquisition system, prior to the SCC testing to obtain the accurate results from the SSR unit.

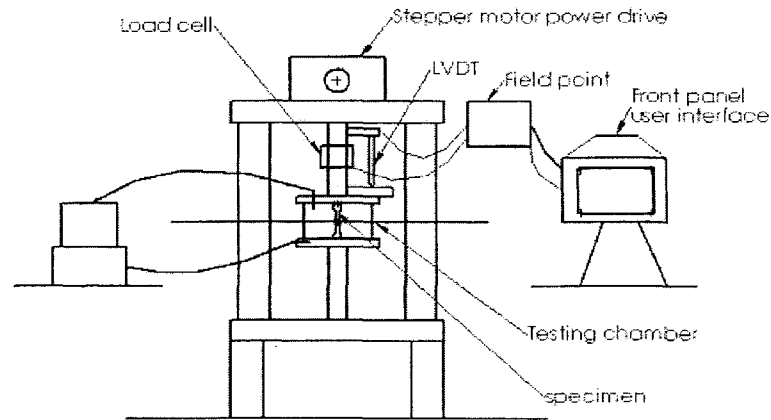


Figure 3.5. SSR Test Setup with Accessories

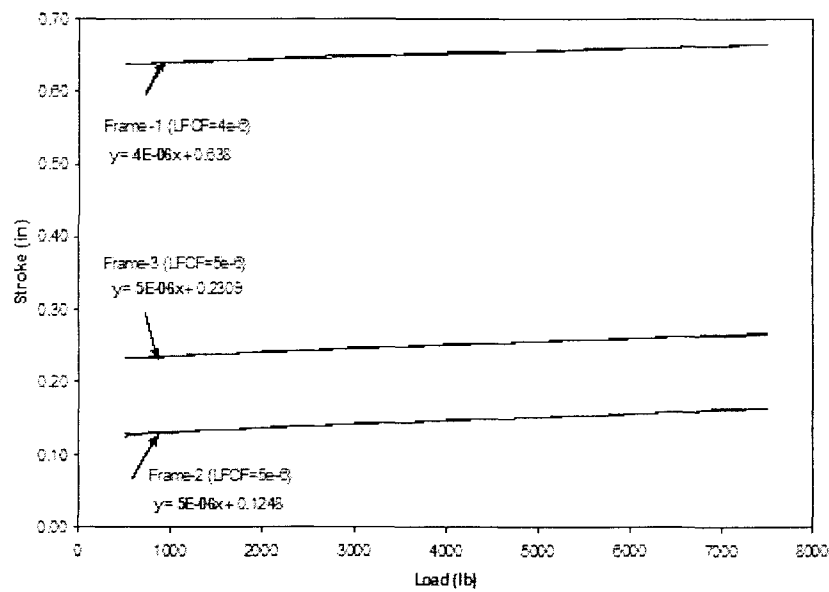


Figure 3.6. Load Frame Compliance Test Results

A strain rate of $3.3 \times 10^{-6} \text{ sec}^{-1}$ was used during the SSR testing. This strain rate was selected based upon prior research work performed at the Lawrence Livermore National Laboratory (LLNL).^(29, 30) SCC occurrence is an effect of two significant factors including the applied/residual stress and a susceptible environment. If the stress is applied

at a very fast rate to the test specimen exposed to an aqueous environment, the resultant failure may not be different from the conventional mechanical deformation produced without an environment. On the other hand, if the strain rate is too slow, the resultant failure may simply be attributed to the corrosion damage due to environmental interaction with the material, thus, causing breakdown of the protective oxide film. In view of this rationale, the SSR testing at LLNL was initially conducted at strain rates ranging between 10^{-5} and 10^{-7} sec^{-1} . Based upon this experimental work, it was determined that a strain rate of around 10^{-6} sec^{-1} would provide the most effective contributions of both the mechanical and environmental factors in characterizing the cracking susceptibility by the SSR method.⁽³¹⁾

The susceptibility of Zr-2 to SCC was evaluated by using both smooth and notched cylindrical specimens. The load versus displacement diagram was generated during these tests and consequently, the engineering stress versus engineering strain diagram for Zr-2 was developed. The dimensions (length and gage diameter) of the test specimens before and after testing were measured. During the SSR testing, the test specimens were subjected to a continuously changing stress. Hence, the cracking tendency of the test material was characterized by the TTF, and the ductility parameters such as the percent elongation (%El) and percent reduction in area (%RA). Further, the true failure stress (σ_f) was also used to characterize the cracking tendency. The magnitudes of %El, %RA, and σ_f were calculated by using the following equations.

$$\% \text{ El} = \left(\frac{L_f - L_o}{L_o} \right) \times 100 \quad ; L_f > L_o \quad (3.1)$$

$$\% \text{ RA} = \left(\frac{A_o - A_f}{A_o} \right) \times 100 \quad ; A_o > A_f \quad (3.2)$$

$$\sigma_f = \frac{P_f}{A_f} \quad (3.3)$$

$$A_o = \frac{\pi \times D_o^2}{4} \quad (3.4)$$

$$A_f = \frac{\pi \times D_f^2}{4} \quad (3.5)$$

Where,

A_o = Initial Cross Sectional Area

A_f = Cross Sectional Area at Failure

P_f = Failure Load

σ_f = True Failure Stress

L_o = Initial Gage Length

L_f = Final Gage Length

D_o = Initial Diameter

D_f = Final Diameter

3.4. Localized Corrosion Evaluation.

Electrochemistry plays an important role in understanding the corrosion mechanism of metallic materials. The use of polarization techniques can provide significant information on the corrosion mechanisms, corrosion rate and susceptibility of materials to localized corrosion in different environments. The equilibrium conditions existing during an electrochemical reaction can be disturbed by applying either an external potential or

current. This phenomenon is known as polarization. The magnitude of polarization is generally described by an overvoltage (η), which is a measure of polarized potential with respect to the corrosion potential (E_{corr}) of an electrode.⁽³²⁾ The magnitude of η can be either positive or negative depending on the applied electrochemical potential during the polarization of a metallic specimen of interest. The η is given by the following equation.

$$\eta = E_{\text{app}} - E_{\text{corr}} \quad (3.6)$$

Where,

E_{app} = Applied electrochemical potential

E_{corr} = Corrosion/open-circuit potential

The magnitude of η is positive for an anodic polarization while a negative η signifies a cathodic polarization.

Cyclic potentiodynamic polarization (CPP) is a testing technique by which the anodic polarization of a metallic alloy can be performed in a cyclic manner. It is often used to evaluate the susceptibility of a material to pitting corrosion, which is usually characterized by a change in slope during the forward potential scan at a potential known as critical pitting potential (E_{pit}). At this potential, the material undergoes localized breakdown of its protective surface film causing initiation of pits. Materials that are capable of repassivation by formation of a protective film during the reverse potential scan are characterized by a potential known as repassivation/protection potential (E_{prot}), as shown in Figure 3.7. The larger the difference between E_{pit} and E_{prot} , the greater is the resistance of the material to localized attack, in particular, to pitting corrosion.

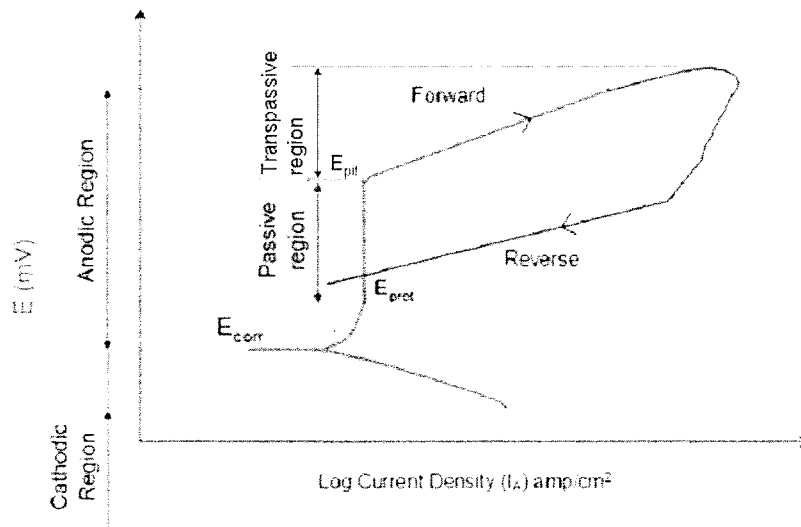


Figure 3.7. CPP Diagram for an Active-Passive Material

The CPP experiments involving small cylindrical specimens of Zr-2 were performed in the test solution at 30 and 90°C using a GAMRY PCI4 potentiostat. A potentiostat is an electronic device, which can control the potential between the working and reference electrodes. The measured potential is known as the corrosion or open-circuit potential (E_{corr}). During polarization of the test specimen, electron flow can occur between the test specimen and the counter electrode due to the application of potential at a constant rate, thereby producing a non-equilibrium condition.

The GAMRY potentiostat was calibrated according to the ASTM designation G 5⁽²²⁾ prior to the performance of the CPP experiment. The purpose of this calibration was to generate a characteristic polarization diagram using a ferritic type 430 stainless steel specimen in a 1 normal (1N) sulfuric acid (H_2SO_4) solution at 30°C at a potential scan rate of 0.17 mV/sec. This potentiostat was considered to be functioning accurately if the generated calibration curve exhibited a pattern similar to that of the ASTM curve,

showing somewhat similar critical potential values. For CPP testing using this potentiostat, a three-electrode polarization method was used. This technique consisted of the test specimen as the working electrode (anode), two graphite electrodes as the cathodes and silver/silver chloride (Ag/AgCl) as the reference electrode. The reference electrode was contained in a luggin probe in such a way that the tip of the probe was placed within 2-3 mm away from the specimen surface, as shown in Figure 3.8. The experimental setup used in the CPP testing is shown in Figure 3.9.

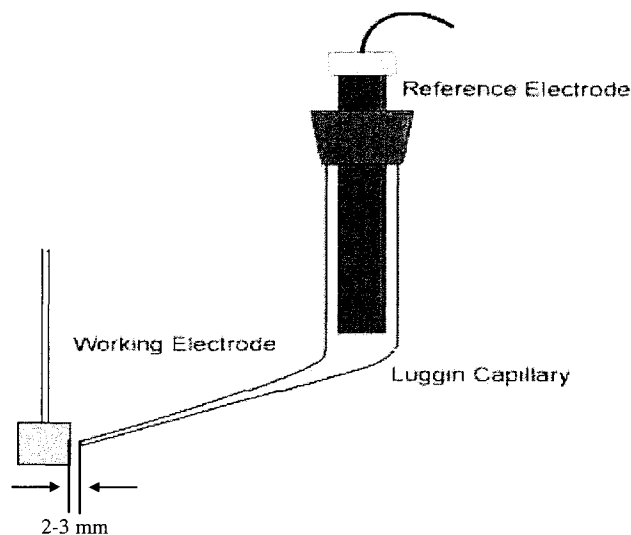


Figure 3.8. Luggin Probe Arrangement

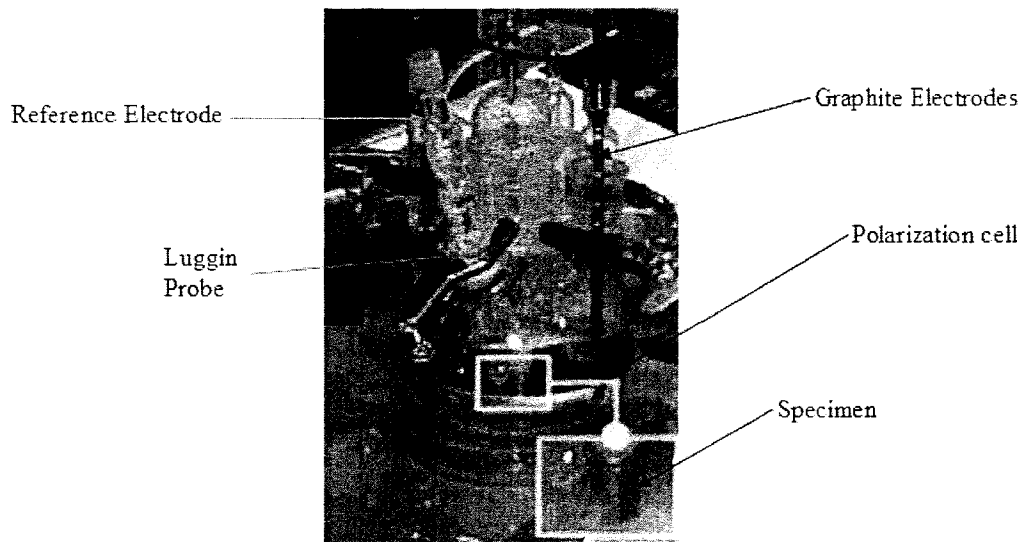


Figure 3.9. CPP Test Setup

3.5. SCC Testing Under E_{cont}

It is well known ⁽¹²⁾ that the application of either an anodic or cathodic potential to a test specimen can accelerate the cracking tendency in a susceptible environment while the specimen is loaded in tension. In order to evaluate the effect of controlled electrochemical potential (E_{cont}) during the straining of cylindrical specimens by the SSR technique, both cathodic and anodic E_{cont} values were applied. The magnitude of E_{cont} during cathodic potentiostatic polarization was based on the E_{corr} value of Zr-2 obtained in a similar test environment. On the other hand, the magnitude of E_{cont} in anodic polarization experiments was based on the E_{pit} value in a similar environment. In essence, a potential active (negative) to the E_{corr} value was used in potentiostatic SCC testing under cathodic control. Conversely, the E_{cont} value used in anodic potentiostatic experiments was noble (positive) with respect to the E_{pit} value.

For SCC testing under E_{cont} , the cylindrical specimen was spot-welded at its top shoulder with a conductive metallic wire for application of potential from the potentiostat. This wire was coated with a lacquer to prevent its contact with the test solution during straining under E_{cont} . The experimental setup used in potentiostatic SCC testing is shown in Figure 3.10.

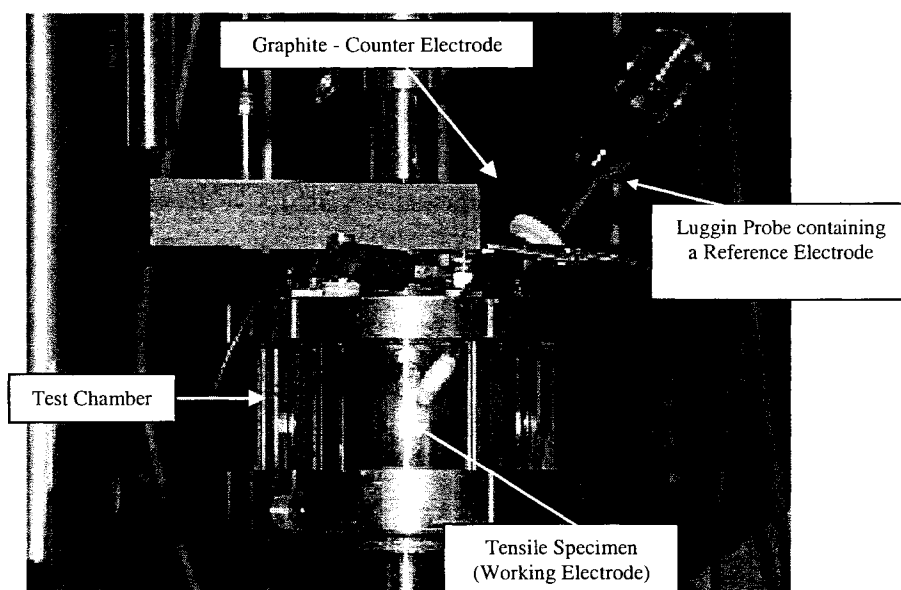


Figure 3.10. SCC Test Setup under Controlled Potential

3.6. Optical Microcopy

The metallographic technique using an optical microscope enables the characterization of phases present, their distribution within grains, and their sizes that can depend on the chemical composition and thermal treatments performed on a material of interest. The principle of an optical microscope is based on the impingement of a light source perpendicular to the surface of the test specimen. The light rays pass through a system of condensing lenses and shutters, up to a half-penetrating mirror. This brings the

light rays through the objective to the surface of the specimen. Light rays reflected off the surface of the sample can then return to the objective, where they are gathered and focused to form the primary image. This image is then projected to the magnifying system of the eyepiece. The contrast observed under the microscope can result from either an inherent difference in intensity or wavelength of the light absorption characteristics of the phases present. It may also be induced by preferential staining or attack of the surface by etching with a chemical reagent.

The metallurgical microstructure of Zr-2 was evaluated by standard metallographic techniques, which included sectioning of the specimen, mounting it in a castable epoxy resin, grinding and polishing it using polishing cloths. The polished specimens were then etched in proper chemical reagent to expose the specimen surface preferentially. The composition of the etchant used is shown in Table 3.1. The etched specimens were then examined using a LEICA microscope having a resolution capability of 1000 X. The optical microscope used for microstructural evaluation is shown in Figure 3.11.

Table 3.1. Composition of Etchant and Applying Procedure

Constituents	HF (48%)	HNO ₃ (70%)	H ₂ O	Immerse Sample Face Up: Etch
	4-5%	30-35%	Balance	10-15 min and air dry.

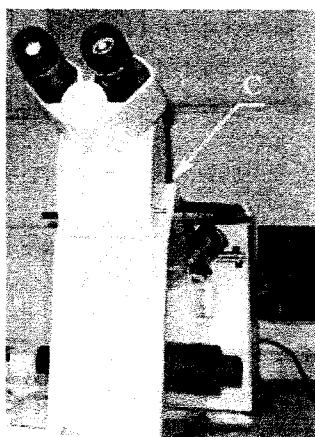


Figure 3.11. LEICA Optical Microscope

3.7. Scanning Electron Microscopy

In a scanning electron microscope (SEM), electrons from a metal filament are collected and focused just like light waves into a narrow beam. The beam scans across the subject, synchronized with a spot on a computer screen. Electrons scattered from the subject are detected creating a current, the strength of which makes the spot on the computer brighter or darker. This creates a photograph-like image with an exceptional depth of field. Magnifications of several thousand times are possible. Normally, SEM provides black and white micrographs. A JEOL-5600 SEM, as shown in Figure 3.12, was used for fractographic evaluation of the tested specimens. This SEM was able to accommodate four samples of different diameters. In addition, it was capable of resolution up to 50 nm at the maximum magnification of 10^5 . The test specimens were sectioned to the desired length and subjected to SEM examination using the conventional technique. The extent and characteristics of failure were determined by this technique.

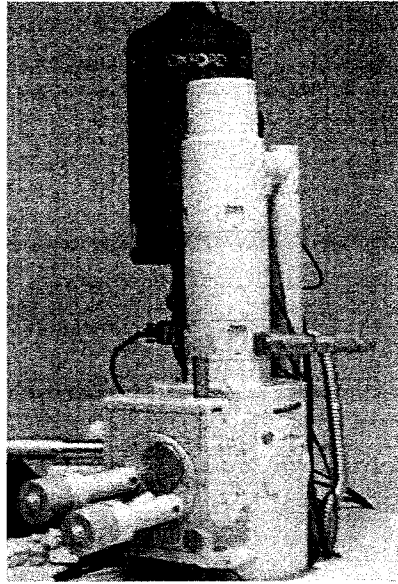


Figure 3.12. JEOL-5600 Scanning Electron Microscope

CHAPTER 4

RESULTS

4.1. Ambient-Temperature Tensile Testing

The results of tensile testing involving smooth and notched cylindrical specimens of zircaloy-2 (Zr-2) using the MTS machine are shown in Table 4.1. An examination of the tensile data on smooth specimens based on Table 4.1 and the vendor's data indicated that the magnitude of yield strength (YS), ultimate tensile strength (UTS), and percent elongation in length (%El) was very close to each other. For example, the YS value of Zr-2 lies around 53 ksi in both cases. Similarly, the UTS value ranged between 76 and 78 ksi. The uncertainty analysis for the YS of the tensile data is shown in Appendix C.

Table 4.1. Ambient Temperature Mechanical Properties

Material/Heat No.	Specimen Geometry	YS, ksi /(Mpa)	UTS, ksi /(Mpa)	%El	%RA
Zr-2/242831	Smooth	53.0 /(365.8)	76.2 /(525.4)	31.0	27.9
	Notched	119.89 /(826.6)	130.8 /(901.6)	NA	NA

4.2. Constant-Load SCC Testing

The results of SCC testing of Zr-2 in the acidic solution at ambient temperature, 60 and 90°C using smooth and notched cylindrical specimens are given in Table 4.2. This data indicate that Zr-2 did not exhibit any failure at applied stresses equivalent to 98% of its YS value using the smooth specimens. Thus, the threshold stress (σ_{th}) for stress-corrosion-cracking (SCC) in this environment may lie in the vicinity of 0.98 YS. The presence of notch in the gage section of the cylindrical specimens however reduced the magnitude of the threshold load (L_{th}) to 70% of its yielding load, as expected. These overall data in terms of σ_{th} , or L_{th} are consistent with the data generated by previous investigators. [23, 24] The reduction in the threshold load in the presence of a notch can be attributed to the stress concentration factor at the root of the notch.

Table 4.2. Results of the CL SCC Tests

Specimen Geometry	Environment, Temperature (°C)		% Applied Stress/Applied Load (lb)*	Result
Smooth	Acidic Solution	30	98% YS/ 2487.22	NF
		60	98% YS/ 2487.22	NF
		90	98% YS/ 2487.22	NF
		90	98% YS/ 2487.22	NF
Notched		90	70% YL/ 1763.93	NF

NF: No Failure

* 1 lb = 0.4545 kg

4.3. Slow-Strain-Rate SCC Testing

The cracking susceptibility of smooth specimens of Zr-2 using the slow-strain-rate (SSR) technique in the acidic solution at ambient and elevated temperatures are shown in Figure 4.1 in the form of engineering stress versus engineering strain (s-e) diagrams. The s-e diagram for Zr-2 tested in air is also superimposed in this figure for comparison

purposes. The data shown in this figure are reproduced in Table 4.3, showing the value of failure strain (ϵ_f), true failure stress (σ_f), time-to-failure (TTF) and ductility parameters including %El and %RA. These parameters were determined using the s-e curves and the specimen dimensions, before and after testing.

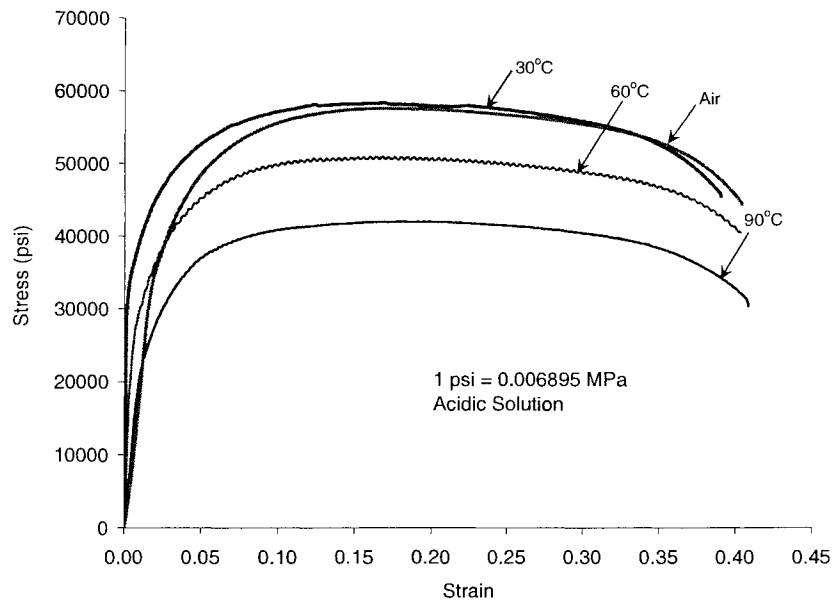


Figure 4.1. Stress versus Strain Diagrams for Smooth Specimens in Acidic Environment

Table 4.3. Results of the SSR SCC Testing using Smooth Specimens

Environment/ Temperature (°C)	%El	%RA	σ_f ksi/(Mpa)	TTF (hr)	ϵ_f
Air/Ambient	39.15	28.92	62.83 /(433.21)	35.30	0.405
Acidic/30	36.36	26.36	62.12/(428.32)	34.0	0.381
Acidic/60	40.53	32.42	56.53/(389.77)	35.16	0.4078
Acidic/90	41.54	33.17	48.95/(337.51)	35.92	0.413

An evaluation of these data indicates that the magnitude e_f was gradually enhanced to some extent at elevated temperatures even in the presence of an acidic solution. These results may suggest that the ductility of Zr-2 maybe enhanced at elevated temperatures while being strained in an acidic solution. This observation is in contrast to the general principles of stress-corrosion-cracking (SCC) phenomenon, which is commonly associated with reduced ductility due to the combined effect of applied stress and a susceptible environment at elevated temperatures. It is possible that the acidic solution used in this investigation may be benign even at elevated temperatures. Further, this increased e_f value at elevated temperature maybe due to the creep deformation showing enhanced plasticity. The magnitude of %El and %RA was also increased at higher testing temperatures to be consistent with the increased e_f .

There are indications ⁽¹²⁾ in the open literature that zirconium alloys may undergo increased cracking susceptibility in an aqueous solution containing iodine at temperatures at or above 200°C. The acidic solution tested initially contained chlorides as shown in Table 2.4. In order to study the effect of iodine on the cracking susceptibility of Zr-2, an aqueous environment containing sulfuric acid (H₂SO₄) and sodium iodide (NaI) was used. SSR tests were performed in this environment using smooth specimens at temperatures ranging from ambient to 90°C. Testing could not be performed at a temperature of 200°C due to the temperature limitation of the SSR unit. It is interesting to note that no cracking was observed even in this environment at any tested temperatures. Nevertheless, the magnitude of σ_f was gradually reduced with increasing temperature in both aqueous environments, as anticipated with any conventional SCC testing. The s-e plot generated in the aqueous environment containing iodine is shown in Figure 4.2, once again showing

increased failure strain at 90°C. The magnitude of e_f , TTF and the ductility parameters derived from these plots and specimen dimensions are shown in Table 4.4, showing a trend similar to those obtained in the environment without the presence of iodine.

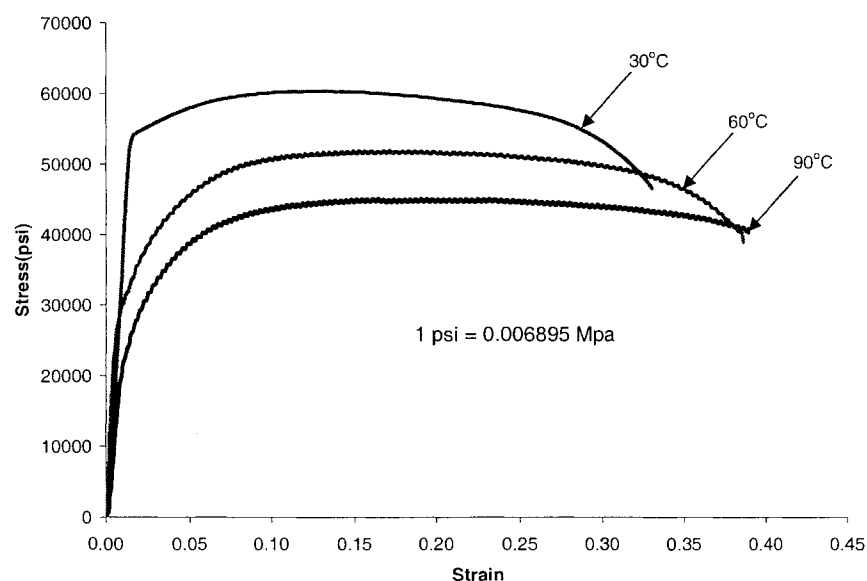


Figure 4.2. Stress versus Strain Diagrams for Smooth Specimens in Iodine Environment

Table 4.4. Results of the SSR SCC Testing in Iodine Environment

Temperature (°C)	%El	%RA	σ_f ksi/(Mpa)	TTF (hr)	e_f
30	35.58	24.84	61.80/(426.11)	29.20	0.330
60	37.45	29.56	55.18/(380.47)	34.21	0.386
90	39.47	31.29	59.36/(409.29)	34.30	0.390

4.4. Effect of Notch on s-e Diagrams in SSR Testing

An effort was made to compare the s-e diagrams, with and without the presence of a notch in the cylindrical specimen using the SSR technique. The s-e diagram for both smooth and notched specimens are superimposed in Figure 4.3, showing enhanced failure stress in the notched specimen due to plastic constraint and triaxial stress condition. However, the failure strain in the smooth specimen was significantly higher due to relatively increased plasticity associated with it. The overall test data obtained from this comparison are shown in Table 4.5.

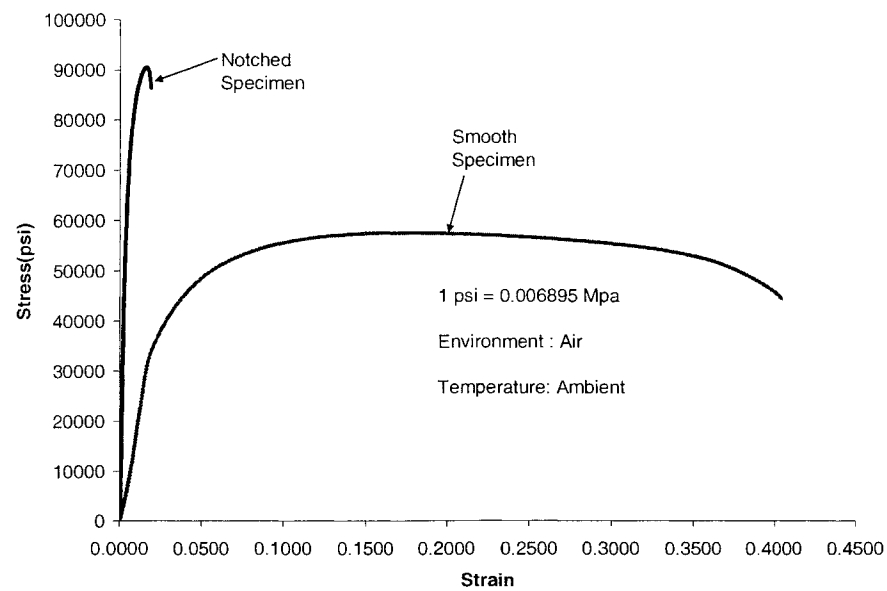


Figure 4.3. Comparison of Smooth and Notched Specimens Tested under SSR Condition

Table 4.5. Results of the SSR Testing using Smooth and Notched Specimens

Environment/ Temperature (°C)	%El	%RA	σ_f ksi/(Mpa)	TTF (hr)	e_f
Air/Ambient	39.15	28.92	62.83/(433.21)	35.30	0.405
Air/Ambient	NA	NA	84.76/(584.42)*	3.32	0.021

* Failure stress for notched specimen is engineering stress

4.5. SSR Testing Under E_{cont}

It is well known ⁽¹²⁾ that the cracking susceptibility of engineering metals and alloys maybe influenced by externally applied potential. In view of this rationale, the cracking susceptibility of Zr-2 was determined in the acidic solution under the influence of both cathodic and anodic controlled potential (E_{cont}). For SCC testing under cathodic E_{cont} , the cylindrical specimens were strained using the SSR technique, while potentiostatistically polarizing them at potentials of -675,-875, and -1000 mV (wrt Ag/AgCl). These E_{cont} values were selected to apply potential active to the measured E_{corr} value in a similar environment. One E_{cont} testing was also performed under a constant loading condition.

The results of SCC testing using cathodic E_{cont} values are illustrated in Figure 4.4, showing a superimposition of s-e diagrams as a function of the applied potentials. An examination of these s-e diagrams indicates that the effect of cathodic E_{cont} on the cracking susceptibility was minimum, showing insignificant variation in the failure strain (e_f). The magnitude of σ_f , e_f , TTF, %El and %RA derived from these plots and specimen dimensions are shown in Table 4.6. An evaluation of this table clearly indicates slight reduction in ductility and σ_f at an E_{cont} value of -1000 mV. These data may suggest a detrimental effect of more active E_{cont} values on the cracking susceptibility of Zr-2.

However, the magnitude of e_f was not changed significantly, as indicated earlier. The variations of the ductility parameters with E_{cont} are shown in Figure 4.5.

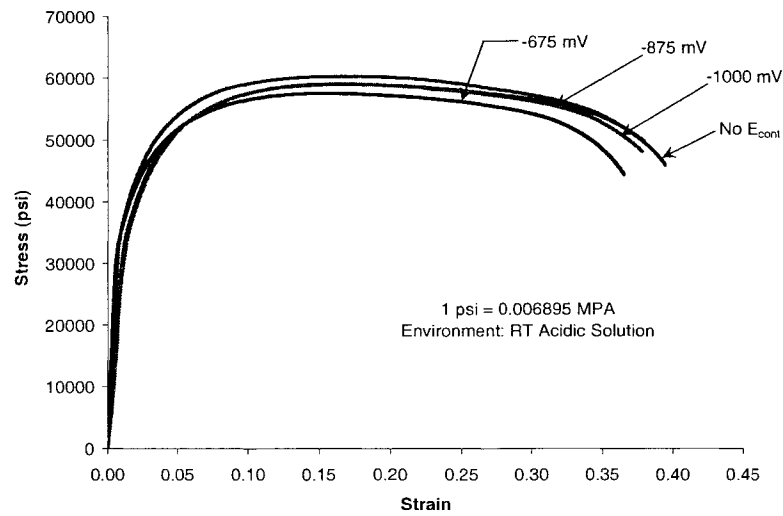


Figure 4.4. Stress-Strain Diagrams for Zr-2 under Cathodic E_{cont}

Table 4.6. Results of the SSR Testing under Cathodic E_{cont}

Applied Potential	%El	%RA	σ_f ksi/(Mpa)	TTF (hr)	e_f
-675 mV	35.35	26.82	66.12/(455.90)	34.28	0.379
-875 mV	34.81	26.27	61.94/(427.04)	33.10	0.378
-1000 mV	33.8	24.69	59.65/(411.29)	33.87	0.378

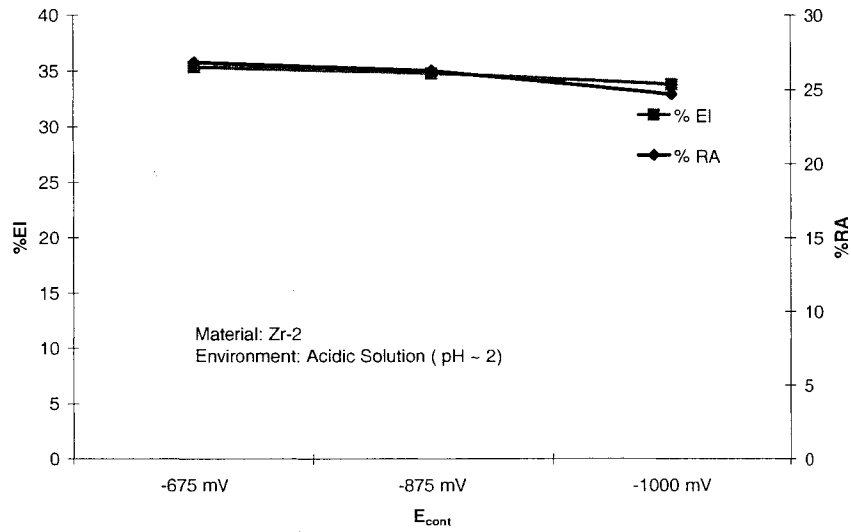


Figure 4.5. E_{cont} Vs Ductility Parameters in SSR Testing

The effect of active E_{cont} on the cracking susceptibility of Zr-2 was also studied at a constant load using a notched cylindrical specimen loaded to 70% of its yielding load for seven days. As indicated earlier, the notched specimen did not exhibit failure at 0.7 YL when tested for thirty days. Since, the E_{cont} testing involving notched specimen was performed only for seven days, it is difficult to make a comparative analysis of the role of the notch on the cracking susceptibility under an active E_{cont} value. Nevertheless, no difference in cracking susceptibility was noted in this single test due to the application of an active E_{cont} to the notched specimen.

Efforts were also made to study the effect of active E_{cont} values on the cracking susceptibility of notched Zr-2 specimens under SSR condition. The s-e diagrams are shown in Figure 4.6, with and without cathodic E_{cont} values. Based on these diagrams, there is an indication that the failure strain may be reduced to some extent due to the combined effect of cathodic E_{cont} and the presence of notch.

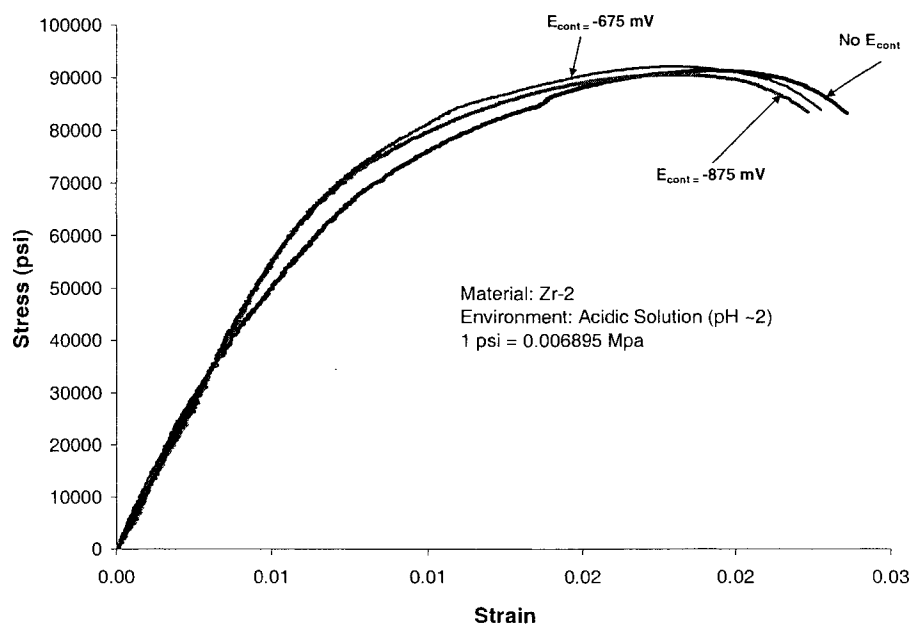


Figure 4.6. Stress-Strain Diagrams for Notched Specimens under Cathodic E_{cont}

As indicated earlier in this thesis, Zr and its alloys may undergo cracking in a susceptible environment due to the application of E_{cont} , noble (positive) to the critical pitting potential (E_{pit}). Therefore SCC testing was performed involving Zr-2 at an E_{cont} value of +500 mV (Ag/AgCl) during its straining under the SSR condition at ambient temperature. The results of SSR testing in room temperature acidic solution involving smooth Zr-2 specimens are shown in Figure 4.7, with and without an anodic E_{cont} value. This figure clearly indicates that the cracking susceptibility of Zr-2 was significantly enhanced in terms of e_f . The data shown in this figure was further analyzed in a tabular format showing the magnitude of %El, %RA, e_f , σ_f and TTF (Table 4.7). Obviously, the ductility and TTF were significantly reduced at anodic E_{cont} values, as shown in this table.

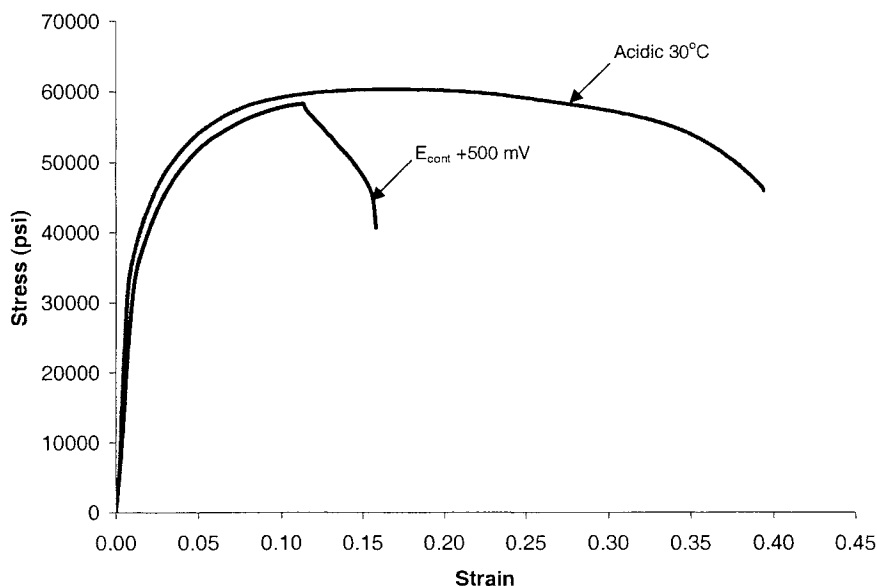


Figure 4.7. Stress-Strain Diagrams under Anodic E_{cont}

Table 4.7. Results of SSR Testing under Anodic E_{cont}

Environment	E_{cont} , mV(Ag/AgCl)	%El	%RA	e_f	σ_f , ksi /(MPa)	TTF (hrs)
Acidic Solution	None	36.36	26.36	0.381	62.12 /(428.32)	33.94
	+500	21.84	16.60	0.172	60.61 /(417.91)	15.90

4.6. Localized Corrosion Study

A GAMRY PCI4 potentiostat was calibrated according to the ASTM method ⁽²²⁾ prior to the performance of cyclic potentiodynamic polarization (CPP) experiments to determine the localized corrosion behavior of Zr-2. A typical potentiodynamic polarization curve generated according to the ASTM standard ⁽²²⁾ is shown in Figure 4.8. If the calibration curve generated by the GAMRY potentiostat matched the shape shown

in Figure 4.8, and the magnitude of E_{corr} , N_1 and N_2 fell within certain specified ranges, then this potentiostat was considered to be functioning accurately. The calibration curve generated by the GAMRY potentiostat is illustrated in Figure 4.9 showing the magnitude of E_{corr} , N_1 and N_2 . A comparison of these parameters to the standard values indicates that all three parameters fell within these specified ranges as shown in Table 4.8. Based on these results, it was construed that the GAMRY potentiostat would provide reliable test results.

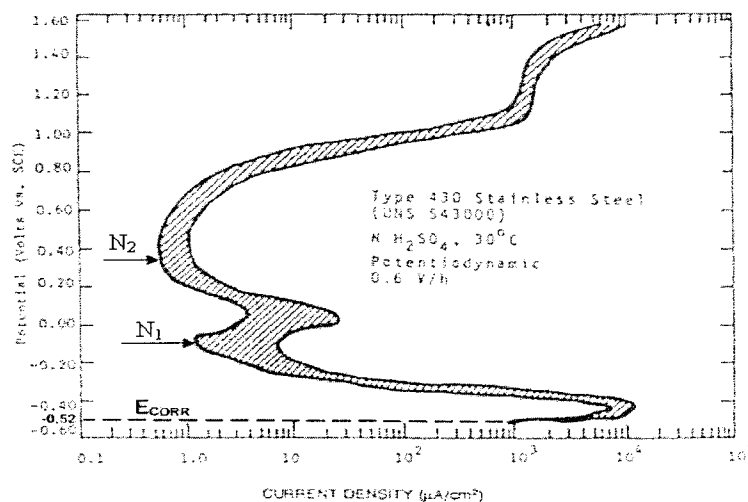


Figure 4.8. Standard ASTM G 5 Potentiodynamic Polarization Curve ⁽²²⁾

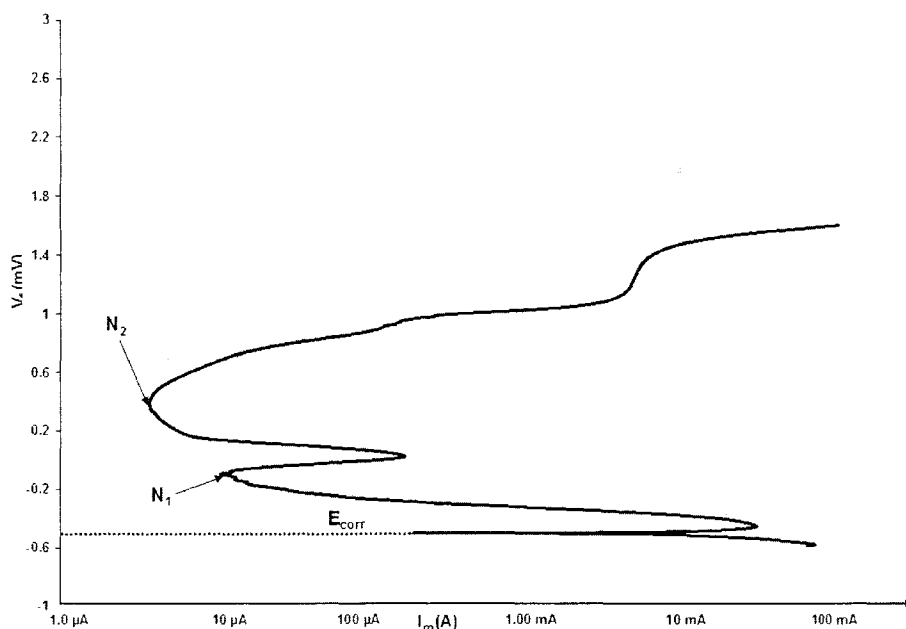


Figure 4.9. Generated ASTM G 5 Potentiodynamic Polarization Curve

Table 4.8. Differences between generated and standard values

	Standard Range (Ag/AgCl)	Actual value (Ag/AgCl)
E_{corr} (mV)	-501 ± 75	-515.9
N_1 (mV)	-51 ± 75	-115.5
N_2 (mV)	411 ± 75	374.5

The resultant CPP diagram using the GAMRY potentiostat are shown in Figures 4.10 and 4.11. These figures identify the magnitude of E_{corr} and E_{pit} in 30 and 90°C acidic solution. Both figures show active-passive behavior as anticipated with Zr alloys. The magnitudes of E_{corr} and E_{pit} determined from these CPP diagrams are shown in Table 4.9.

It is interesting to note that both E_{corr} and E_{pit} became more active at 90°C, as illustrated in Figure 4.12.

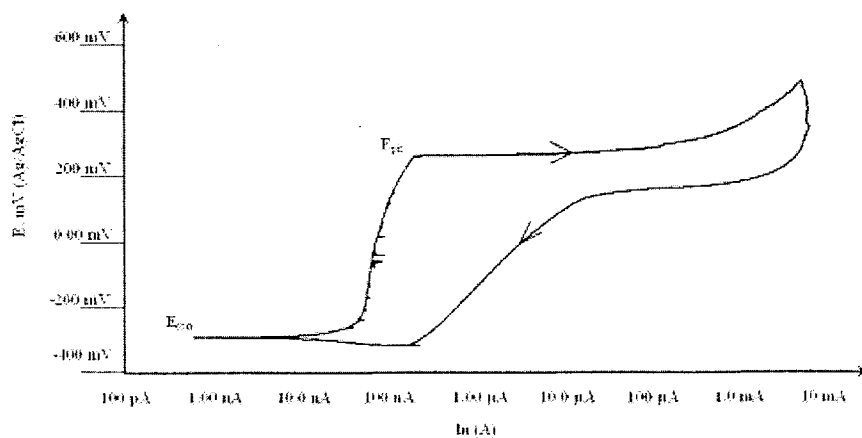


Figure 4.10. CPP Diagram of Zr-2 at 30°C

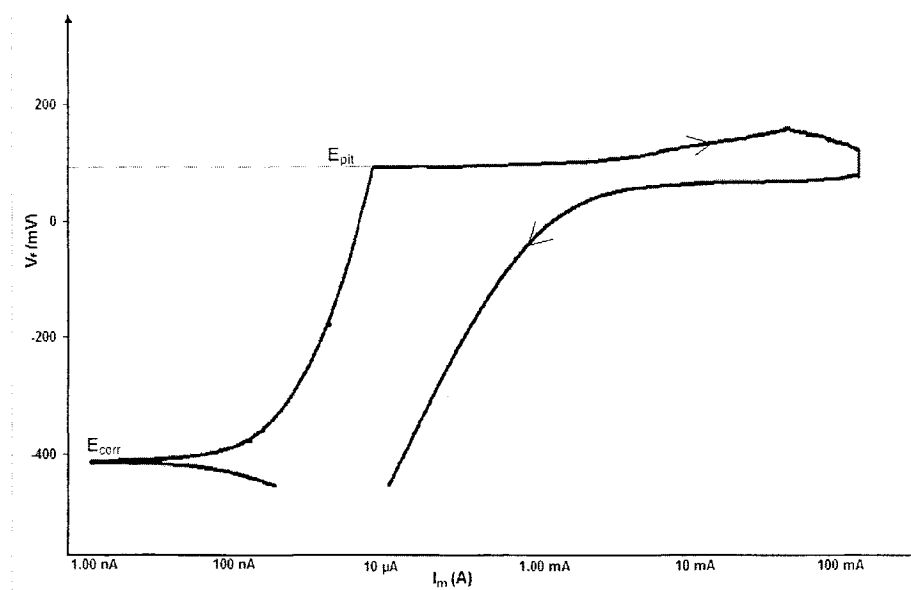


Figure 4.11. CPP Diagram of Zr-2 at 90°C

Table 4.9. Results of CPP testing

Material/Heat No	Temperature	E_{corr} , mV (Ag/AgCl)	E_{pit} , mV (Ag/AgCl)
Zr-2/242831	30°C	-294	243
	90°C	-417	147

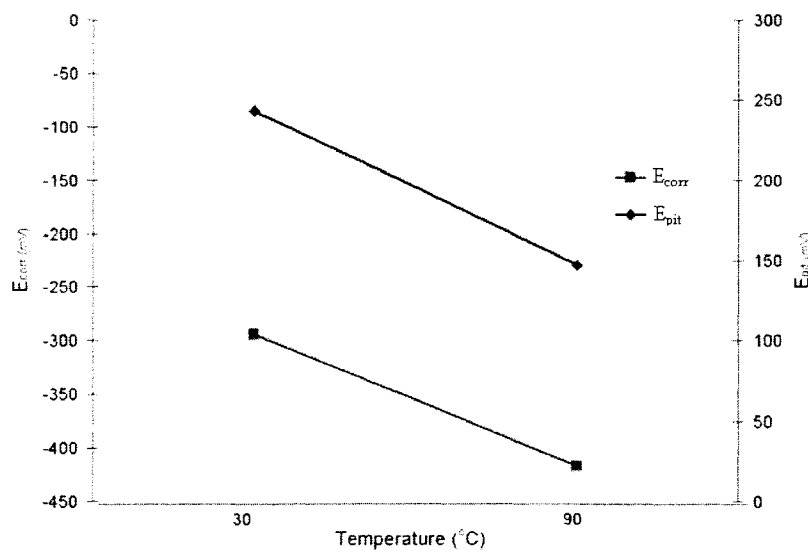


Figure 4.12. Effect of Temperature on Critical Potentials

4.7. Optical Microscopy

The optical micrograph of Zr-2 in a solution-annealed condition is shown in Figure 4.13. An examination of this micrograph obtained in an etched condition reveals the presence of iron-chromium phases precipitated throughout the matrix material. The characteristics of this micrograph is very similar to the microstructure for a zirconium alloy⁽³³⁾ annealed at a temperature comparable to that of the zirconium alloy tested in this

investigation. The typical solution annealing temperature of zirconium alloys is at around 1065°C (1950°F).⁽³⁴⁾ The characteristics of the secondary cracks along the gage section of the tested cylindrical specimens were analyzed by optical microscopy. An optical micrograph showing secondary cracks resulting from SSR testing of Zr-2 in an acidic solution under anodic E_{cont} is illustrated in Figure 4.14.

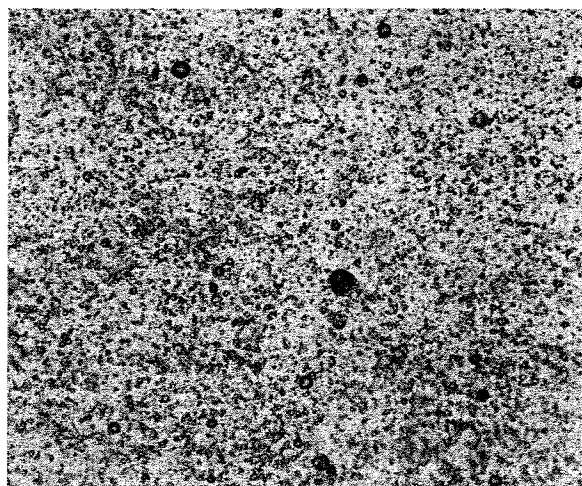


Figure 4.13. Optical Micrograph of Zr-2, HF+HNO₃+H₂O, 100X

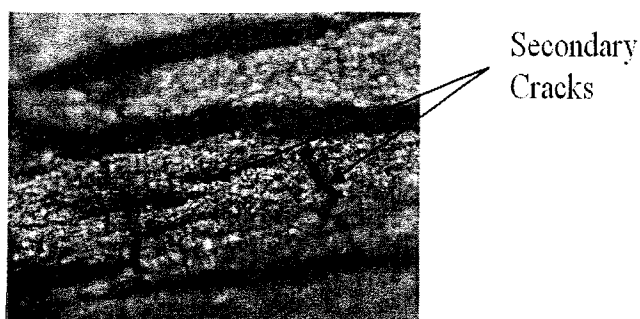
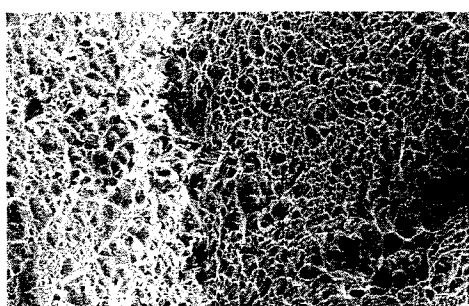


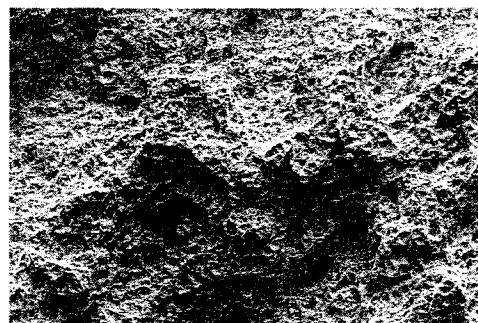
Figure 4.14. Optical Micrograph of Zr-2 Showing Secondary Cracks

4.8. Scanning Electron Microscopy

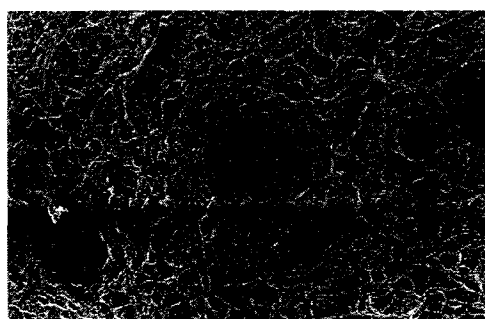
As discussed earlier, the extent and morphology of failure at the primary fracture surface of all cylindrical specimens tested under SSR condition were evaluated by SEM. The results, shown in Figure 4.15, indicate that ductile failure characterized by dimpled microstructures was experienced by Zr-2 specimens irrespective of the testing environment (air versus acidic solution) and temperature. It is interesting to note that Zr-2 exhibited a similar failure mode in the presence of iodine at 90°C, as illustrated in Figure 4.16.



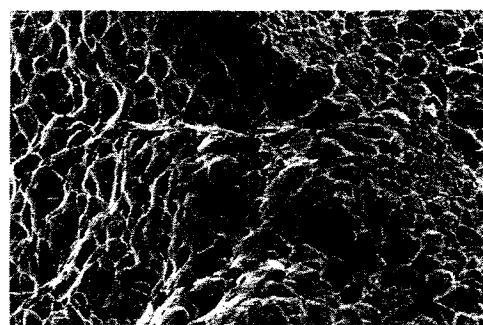
(a) RT, Air



(b) RT, Acidic Solution



(c) 60°C, Acidic Solution



(d) 90°C, Acidic Solution

Figure 4.15. SEM Micrographs of Test Specimens, 150 X

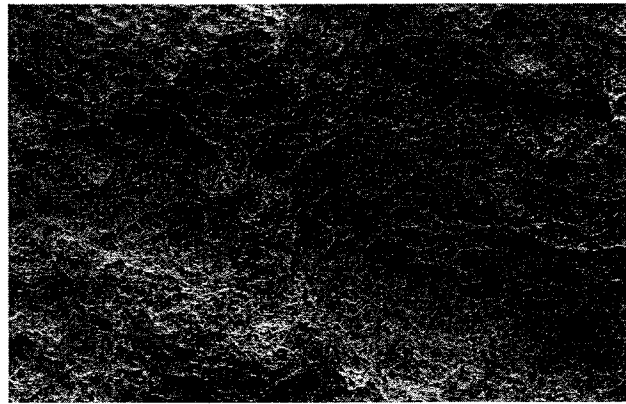
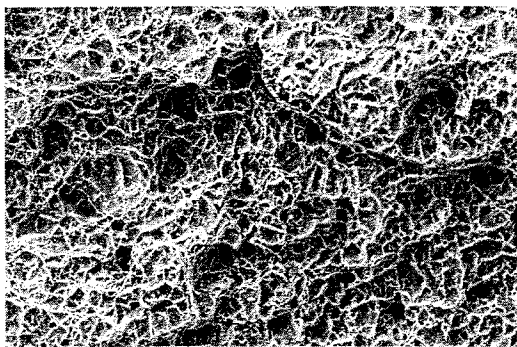
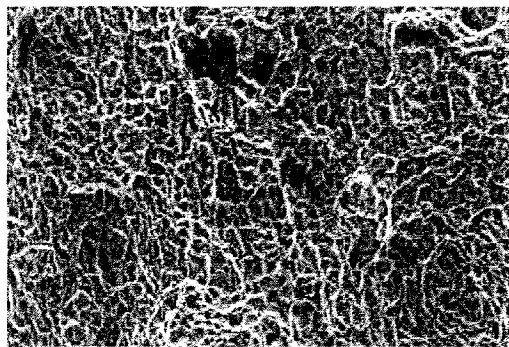


Figure 4.16. SEM Micrographs of Zr-2, 90°C Acidic Iodine Solution, 150 X

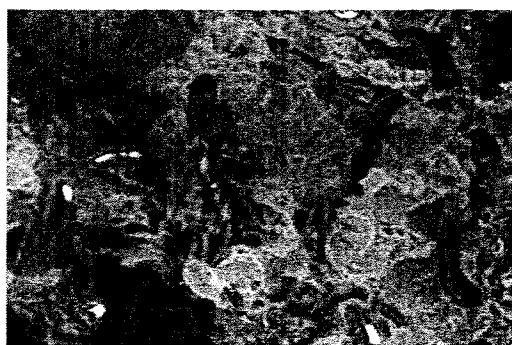
The determination of the failure mode of Zr-2 tested under cathodic E_{cont} (-675, -875 and -1000 mV, Ag/AgCl) by SEM also revealed ductile failures, as shown in Figure 4.17. However, the SEM micrograph of Zr-2 tested under an E_{cont} value of +500 mV (Ag/AgCl) showed the formation of both transgranular and intergranular cracking along the primary fracture surface. It is interesting to note that transgranular cracks were formed at the beginning, followed by branching of these crack along the grain boundaries, as illustrated in Figure 4.18.



(a) $E_{\text{cont}} = -675 \text{ mV (Ag/AgCl)}$



(b) $E_{\text{cont}} = -875 \text{ mV (Ag/AgCl)}$



(c) $E_{\text{cont}} = -1000 \text{ mV (Ag/AgCl)}$

Figure 4.17. SEM Micrographs of Zr-2 under Cathodic Potentials, RT Acidic Solution, 150 X

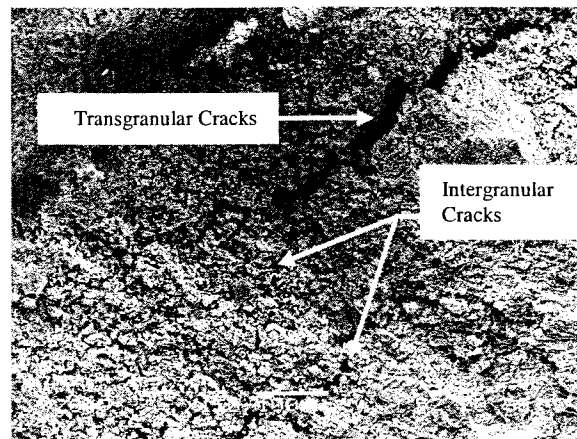


Figure 4.18. SEM Micrograph of Zr-2 under Anodic Potential, RT Acidic Solution,
150 X

CHAPTER 5

DISCUSSIONS

This investigation was focused on the characterization of metallurgical and corrosion behavior of zircaloy-2 (Zr-2), which is a leading cladding material to contain nuclear fuel elements. The determination of tensile properties of Zr-2 using conventional mechanical testing method revealed that the tensile data generated at the laboratory were very similar to those of the vendor, thus, verifying the accuracy of the mechanical testing equipment used in this study. Zr-2 tested in this investigation was received in a solution-annealed condition. Even though, no additional thermal treatments were given to this material, the metallurgical microstructures evaluated by optical microscopy matched those reported in established literature. ⁽³³⁾

The results of SCC testing in an acidic solution at constant-load (CL) revealed that no failure may be experienced by ZR-2 at an applied stress corresponding to 98% of its room temperature YS value. Thus, the threshold stress (σ_{th}) for cracking in this environment may lie at around 0.98YS, which is consistent with the data generated in previous investigations. ^(23, 24)

The cracking susceptibility of Zr-2 in a similar environment, evaluated by the slow-strain-rate (SSR) technique, was expressed in the form of s-e diagram as a function of the testing temperature. The SSR testing data indicate that the ductility and the TTF were increased while the magnitude of σ_f was reduced at elevated temperature.

The reduction of σ_f with increasing temperature in a susceptible environment is universal with most engineering materials due to the reduction in load-bearing capability when subjected to a combined effect of tensile loading and a potent environment. The fact that Zr-2 did exhibit enhanced ductility and TTF at elevated temperature even in the presence of a hostile aqueous environment may suggest that this environment may not be that detrimental to cause SCC in Zr-2.

In view of the above rationale, a limited number of SCC testing was performed in an acidic solution containing iodine at 90°C, as suggested by some investigators. ⁽¹²⁾ However, Zr-2 still exhibited a similar trend in terms of its ductility and TTF. There are indications that zirconium and its alloys may not undergo enhanced cracking susceptibility even in the presence of iodine unless they are exposed to these environments at least at a temperature of 200 °C. Since, the equipment used in SCC testing in the present investigation is capable of operating at temperatures approaching only the boiling point of water, no further testing could be performed using the existing test facility.

Efforts were also made to study the effect of stress concentration on the cracking susceptibility of Zr-2 under both CL and SSR conditions. As expected, the magnitude of threshold load (L_{th}) was significantly reduced approaching 0.7YL in constant load testing due to the presence of a circular notch in the gage section of the cylindrical specimens used in SCC testing. The use of similar notched specimens in SSR testing resulted in enhanced failure stress due to the presence of triaxial stress condition at the root of the notch even though the failure strain was significantly reduced.

The results of cathodic potentiostatic polarization of Zr-2, during straining under a SSR condition indicate that there were slight reductions in the ductility parameters and true failure stress (σ_f) due to application of potentials active to the E_{corr} value. However, very little change in failure strain was noticed in these tests. These results may suggest that hydrogen generated during cathodic E_{cont} testing might have minimal effect in enhancing the cracking susceptibility of Zr-2 in an acidic solution. The presence of a notch in the test specimen did not influence the cracking susceptibility of this alloy even under a controlled potential. Comparatively, the application of an E_{cont} value, noble (positive) to the E_{pit} value of Zr-2, in a similar environment exhibited a significant reduction in ductility parameters, failure strain and time-to-failure. The magnitude of σ_f was also reduced to some extent due to this anodic applied potential. The detrimental effect of anodic applied potential on the cracking susceptibility of zirconium alloys, as observed in this investigation, is consistent with the observations made by other investigators.⁽¹²⁾

The results of localized corrosion study involving Zr-2 using the CPP technique exhibited an active-passive behavior in the polarization diagram, confirming the general observation reported in the open literature. As expected, the magnitude of E_{corr} and E_{pit} became more active due to a change in temperature from ambient to 90°C when tested in a similar environment. The more active critical potentials (E_{corr} and E_{pit}) signify increased localized corrosion susceptibility with increasing temperature. A similar effect of temperature on localized corrosion behavior of engineering materials has been reported elsewhere.⁽³⁵⁾ It is interesting to note that no repassivation behavior was observed at any tested temperature.

The fractographic evaluation of the primary fracture surface of the specimens used in the SSR testing revealed ductile failure, with and without cathodic controlled potential. The ductile failure was characterized by dimpled microstructure. On the contrary, the specimens tested under an anodic E_{cont} predominantly exhibited transgranular cracking followed by some intergranular pattern, as evidenced by the SEM micrographs. Additionally, the optical micrograph of the slow-strain-rate specimens showed secondary cracks along the gage section of the cylindrical specimen tested under anodic E_{cont} condition.

In light of the overall discussion presented in this section, it can be stated that the data generated from this investigation will have some direct impact on the performance of the cladding material during the emplacement of SNF in the proposed geologic repository. For example, the fact that both E_{corr} and E_{pit} became more active at 90°C may suggest that the electrochemical potential of the cladding material may reach similar active potential values with time when the temperature inside the repository may approach approximately 90-100°C. Under this condition, the cladding material may undergo localized attack. Further, during the emplacement period, the electrochemical potential of the cladding material may reach values, more noble compared to the E_{pit} value in the repository environment. This noble potential, along with the residual stresses in the clad material (Zr-2) may cause embrittlement in this alloy, a phenomenon that was demonstrated in this investigation.

CHAPTER 6

SUMMARY AND CONCLUSIONS

The cracking susceptibility of Zr-2 has been evaluated in an acidic solution at ambient and elevated temperatures under both constant-load and slow-strain-rate conditions. The localized corrosion behavior has been studied by an electrochemical polarization technique. The role of applied potentials (anodic/cathodic) on the cracking behavior has also been investigated. The extent and morphology of cracking have been determined by SEM. Optical microscopy was used to evaluate the metallurgical characteristics of Zr-2. The key conclusions made in this study are summarized below.

- No failures were observed with smooth specimens of Zr-2 at constant load. A σ_{th} value of 0.98YS was noted in these specimens. The presence of a notch, however, increased the cracking susceptibility in terms of L_{th} .
- The ductility parameters were enhanced at elevated temperatures during the SSR testing in acidic solutions with and without iodine. However, the magnitude of true failure stress was reduced at elevated temperatures, as expected.
- The magnitude of E_{corr} and E_{pit} became more active at elevated temperature, while showing an active-passive behavior in the polarization diagram, as anticipated.

- The effect of anodic E_{cont} was more pronounced in causing failure in Zircaloy-2 when tested in an acidic solution under a SSR condition. Very little or no changes in the resultant SCC data were observed at cathodic E_{cont} values.
- The SEM micrograph revealed a combination of transgranular and intergranular brittle failures in SSR testing conducted under an anodic E_{cont} . Dimpled microstructures, characteristic of ductile failures, were noted in the failed specimens, with and without cathodic E_{cont} values.
- Secondary cracks were also noted along the gage section of the cylindrical specimens strained under an anodic E_{cont} condition.

CHAPTER 7

SUGGESTED FUTURE WORK

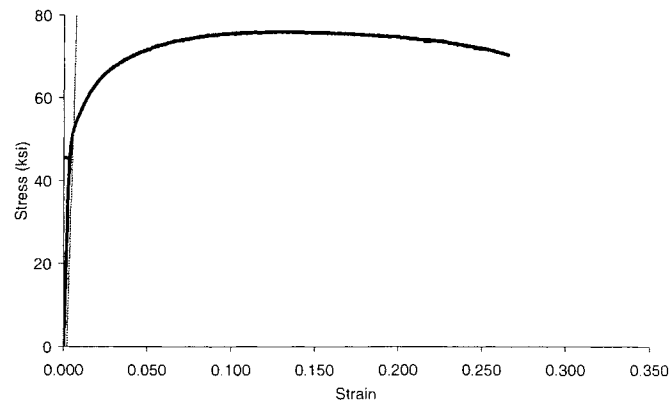
Should funding be available in future, additional work may be performed to address the following issues

- Evaluation of cracking susceptibility in iodine-containing acidic solution at and above 200°C.
- Performance of SCC studies under controlled potentials greater than +500 mV (Ag/AgCl).
- Evaluation of SCC behavior of notched specimen at constant-load under controlled cathodic potential to evaluate the effect of stress concentration for longer durations.

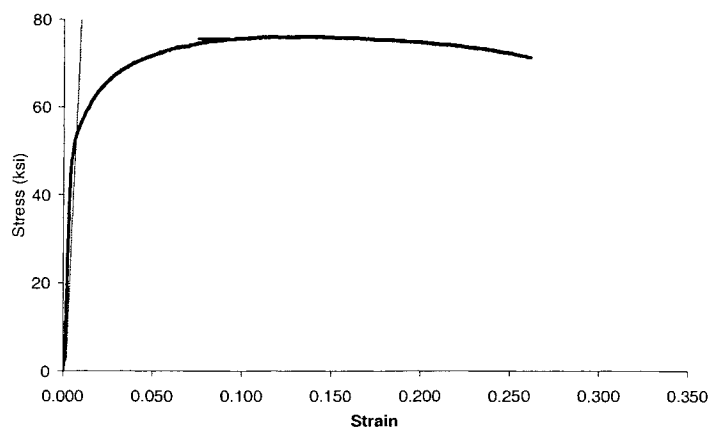
APPENDIX A

TENSILE TESTING DATA

A1. SMOOTH SPECIMENS



Sample 1

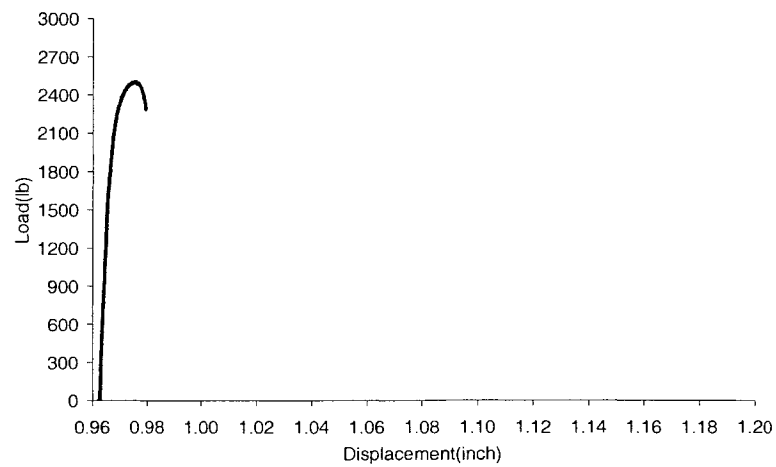


Sample 2

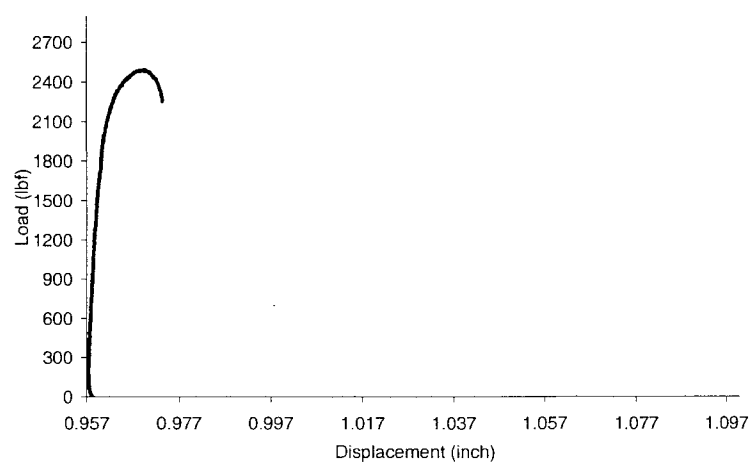
A2. TENSILE TESTING DATA (SMOOTH SPECIMENS)

Material	YS (ksi)	UTS (ksi)	%El	%RA
Zr-2-49	52.5	76.2	30.78	27.33
Zr-2-50	53.6	76.2	31.32	28.38

A3. NOTCHED SPECIMENS



Sample I



Sample 2

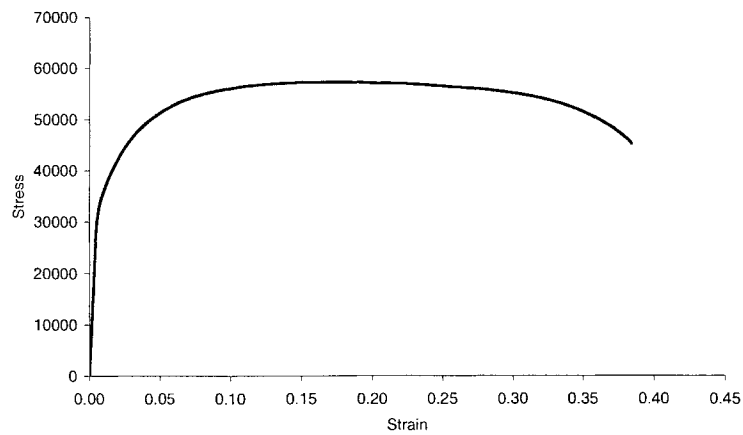
A4. TENSILE TESTING DATA (NOTCHED SPECIMENS)

Material/Heat No.	Specimen ID	YS Ksi/(Mpa)	Ultimate Tensile Strength (Ksi)
Zr-2/242831	26	123.69/(852.84)	130.52/(900)
Zr-2/242831	25	116.09/ (800.44)	131/(903.25)
		119.89/(826.64)	130.76/(901.59)

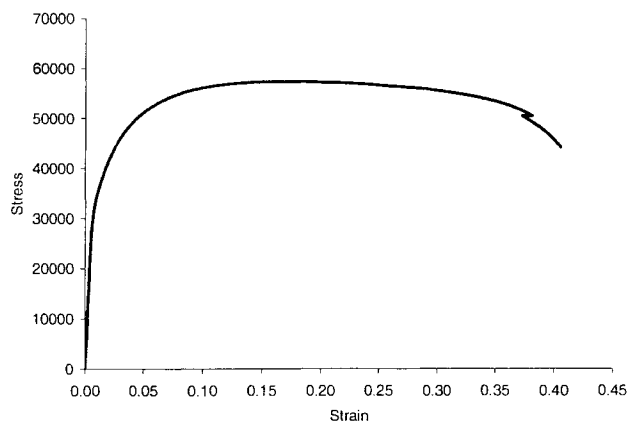
APPENDIX B

SLOW-STRAIN-RATE DATA

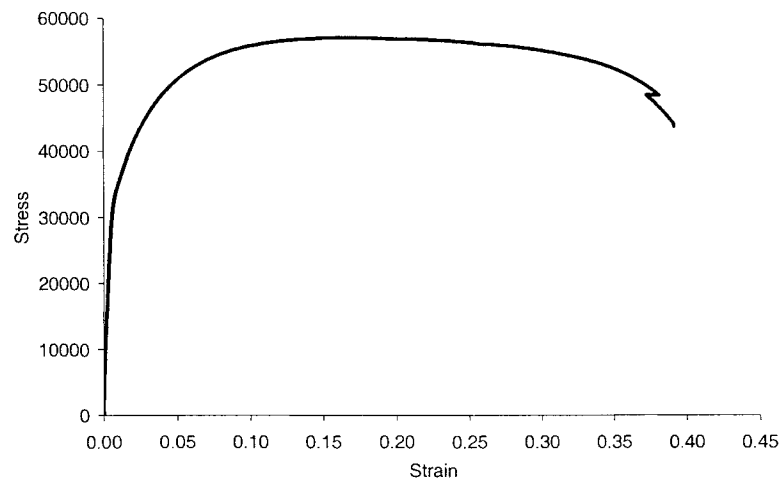
B1.Stress Vs Strain Curves (Smooth Specimens) without E_{cont}



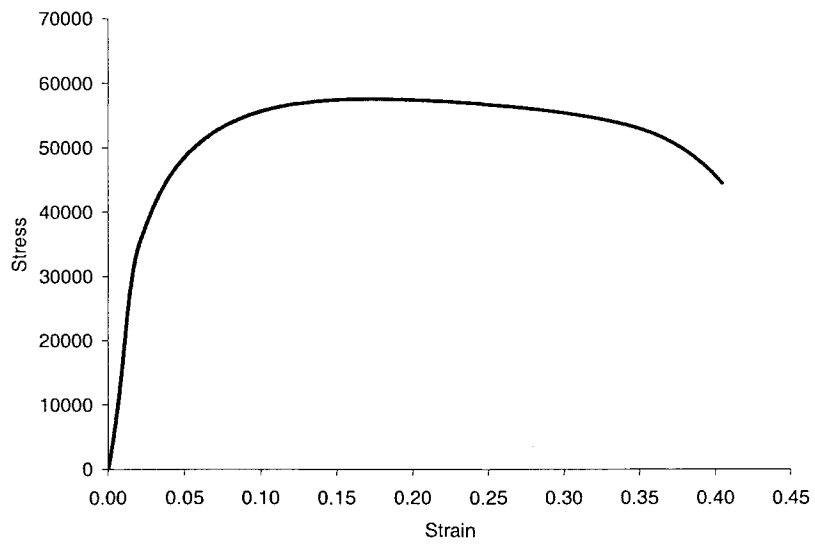
Air (Sample 1)



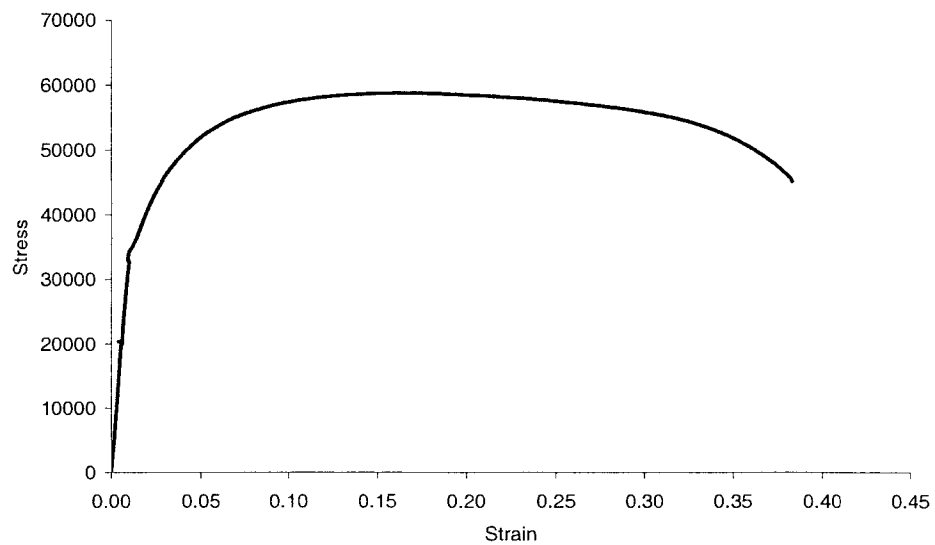
Air (Sample 2)



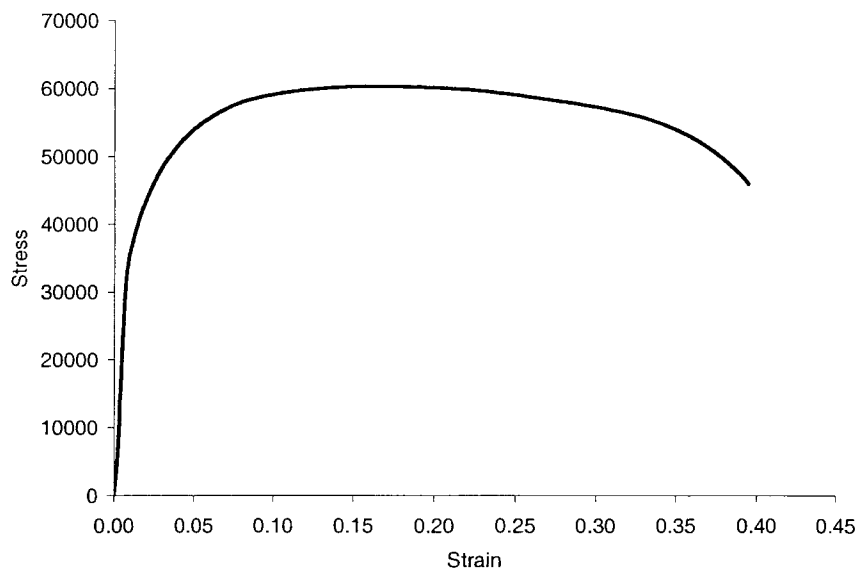
Air (Sample 3)



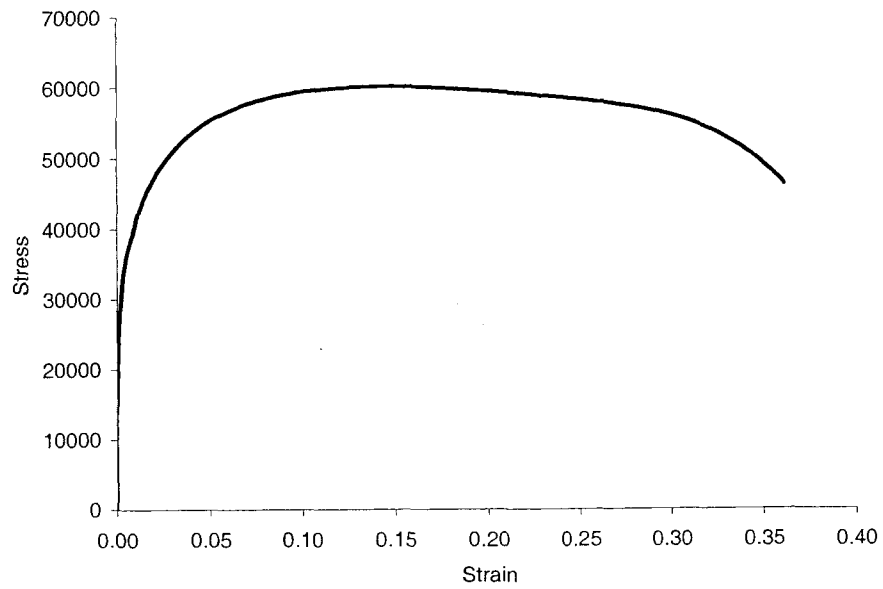
Air (Sample 4)



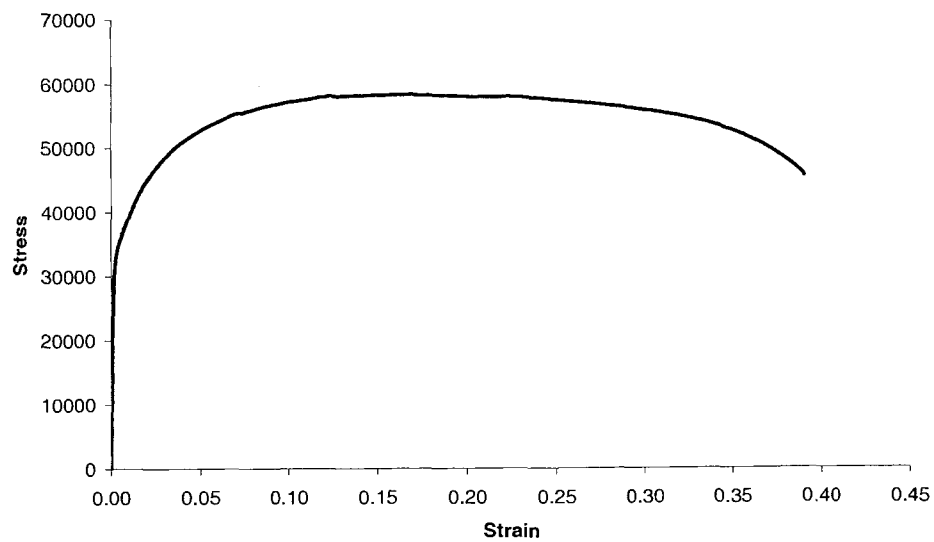
Acidic Environment, Ambient Temperature (Sample 1)



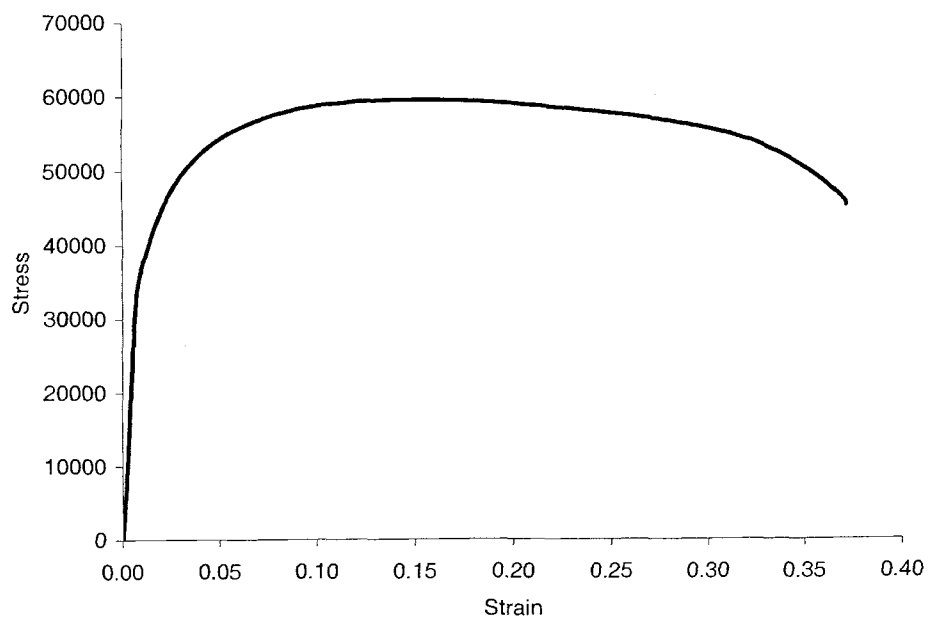
Acidic Environment, Ambient Temperature (Sample 2)



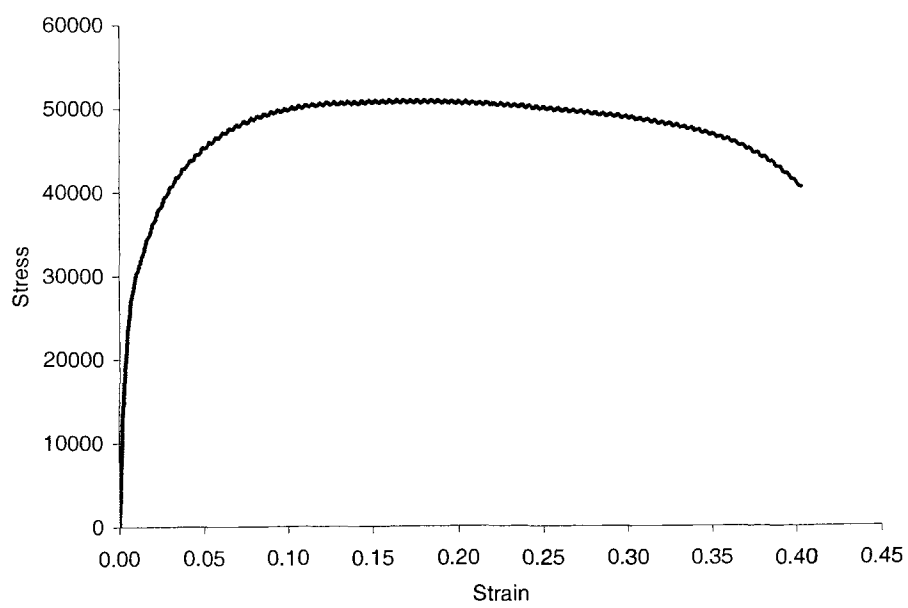
Acidic Environment, Ambient Temperature (Sample 3)



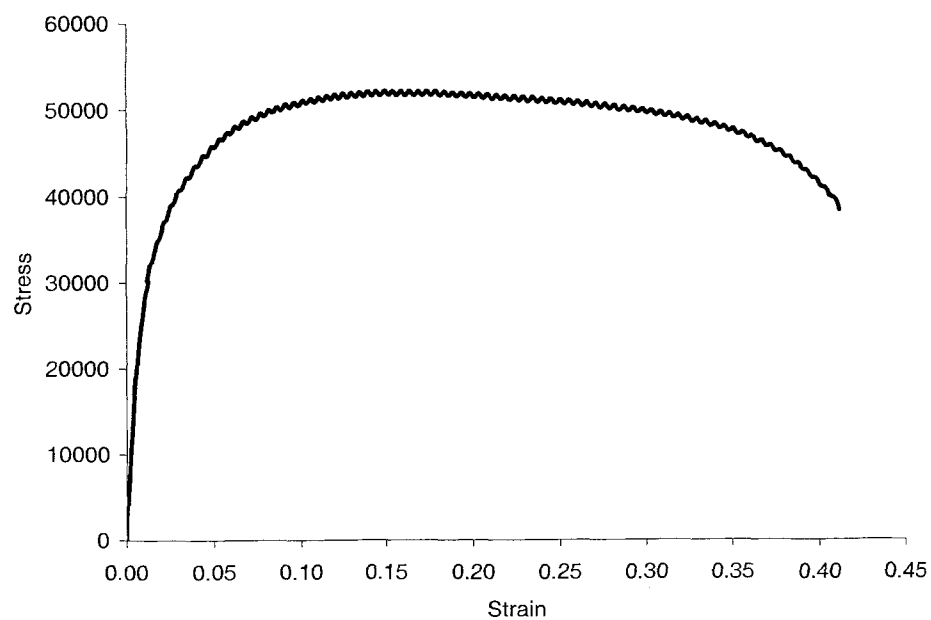
Acidic Environment, Ambient Temperature (Sample 4)



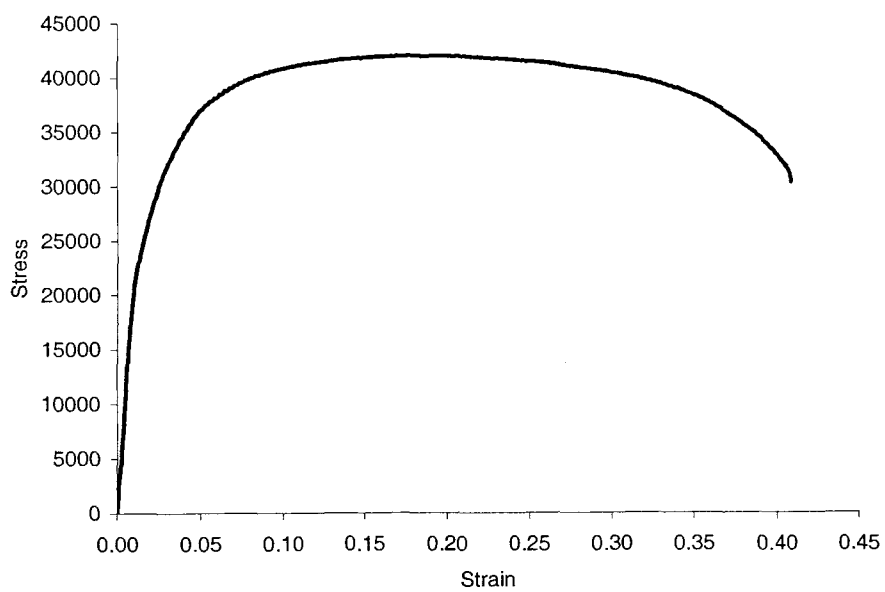
Acidic Environment, Ambient Temperature (Sample 5)



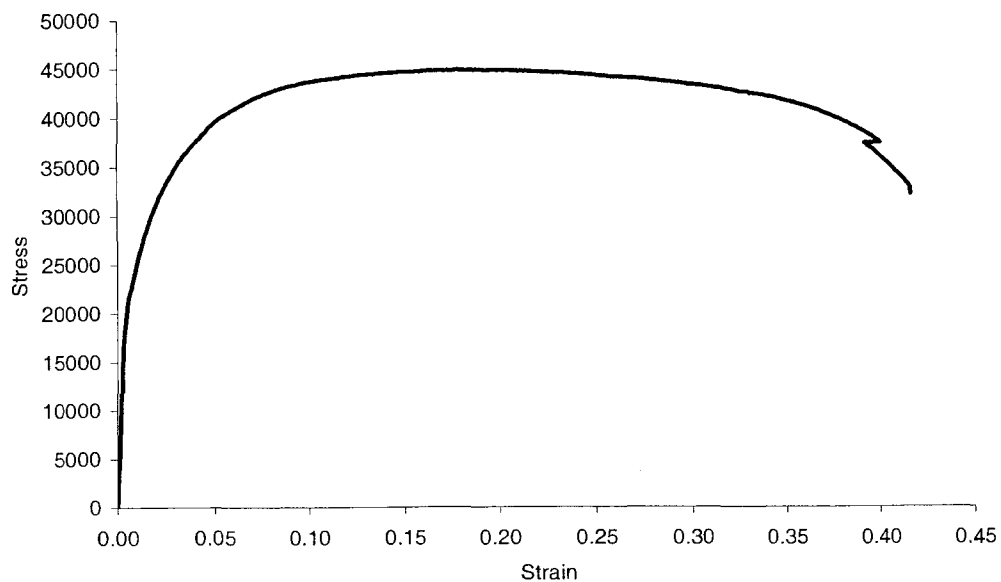
Acidic Environment, 60°C (Sample 1)



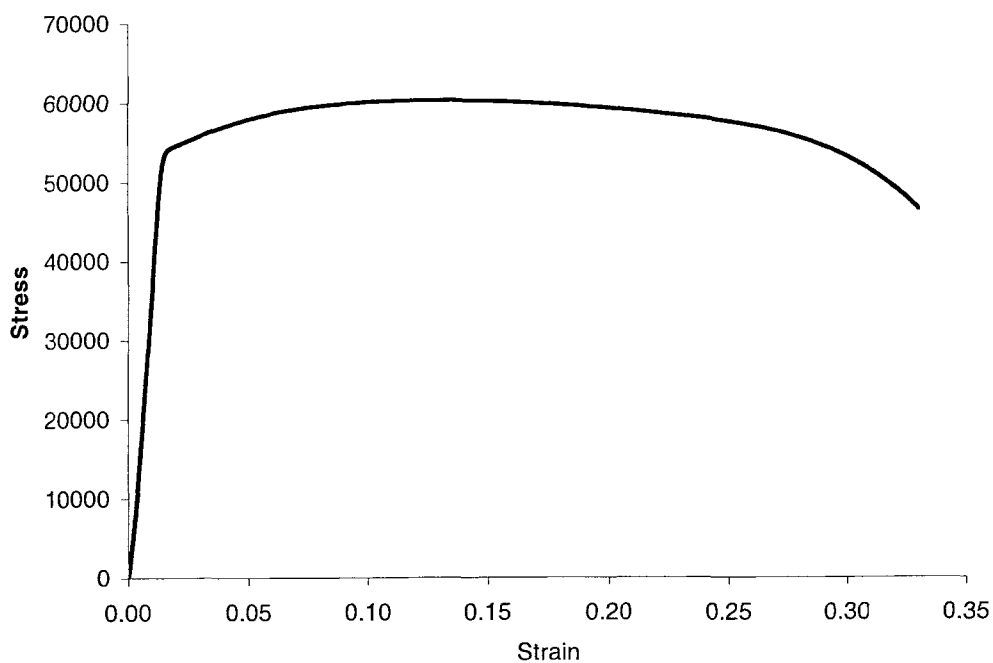
Acidic Environment, 60°C (Sample 2)



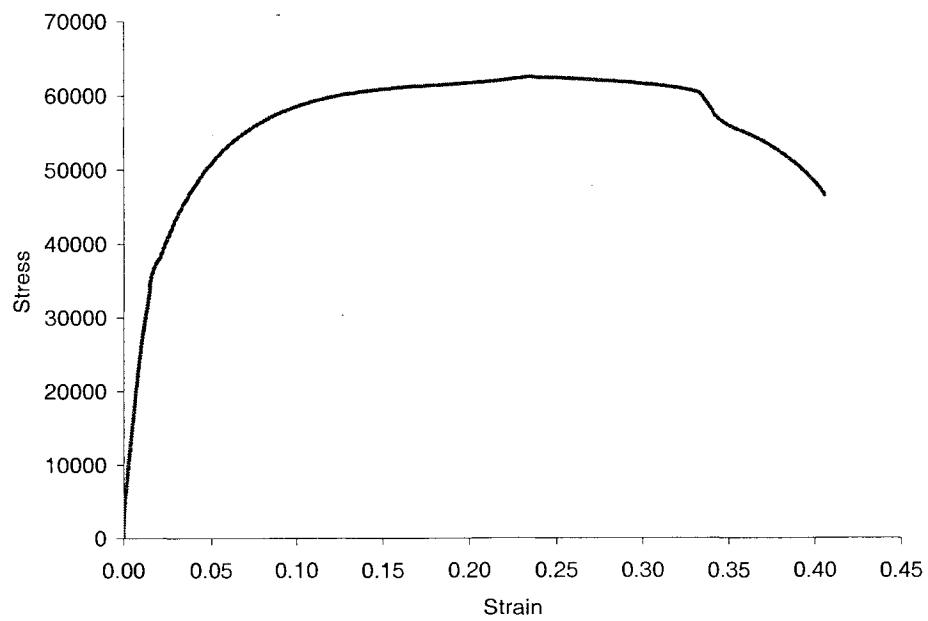
Acidic Environment, 90°C (Sample 1)



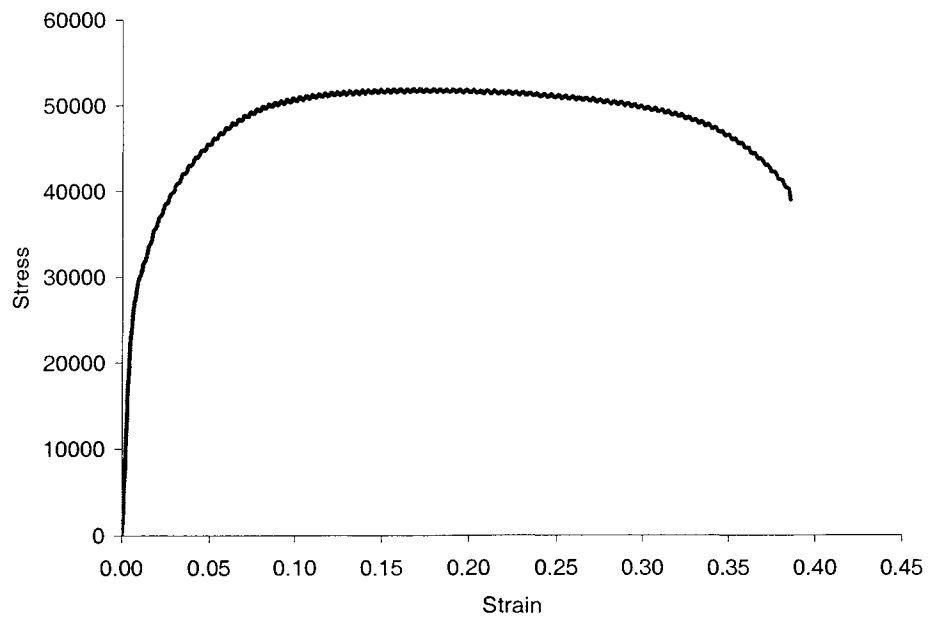
Acidic Environment, 90°C (Sample 2)



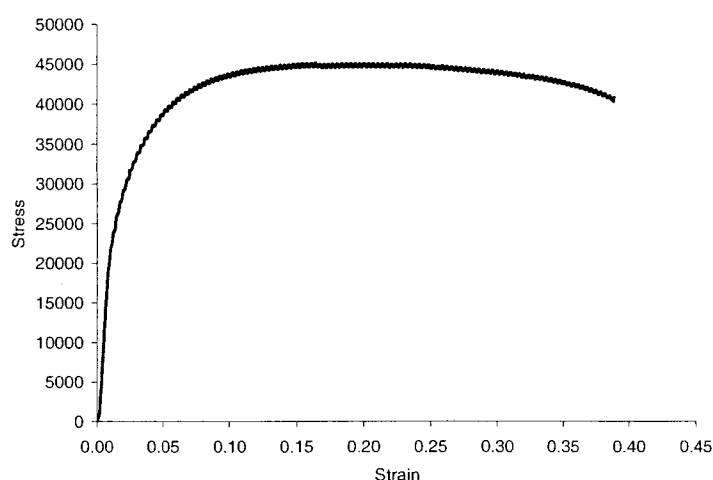
Iodine Environment, Ambient Temperature (Sample 1)



Iodine Environment, Ambient Temperature (Sample 2)



Iodine Environment, 60°C (Sample 1)

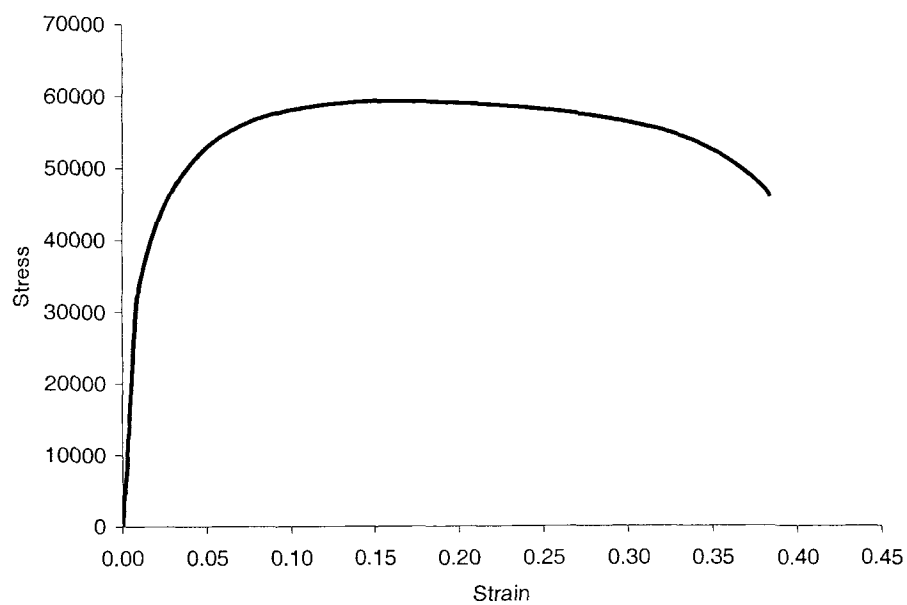


Iodine Environment, 90°C (Sample 1)

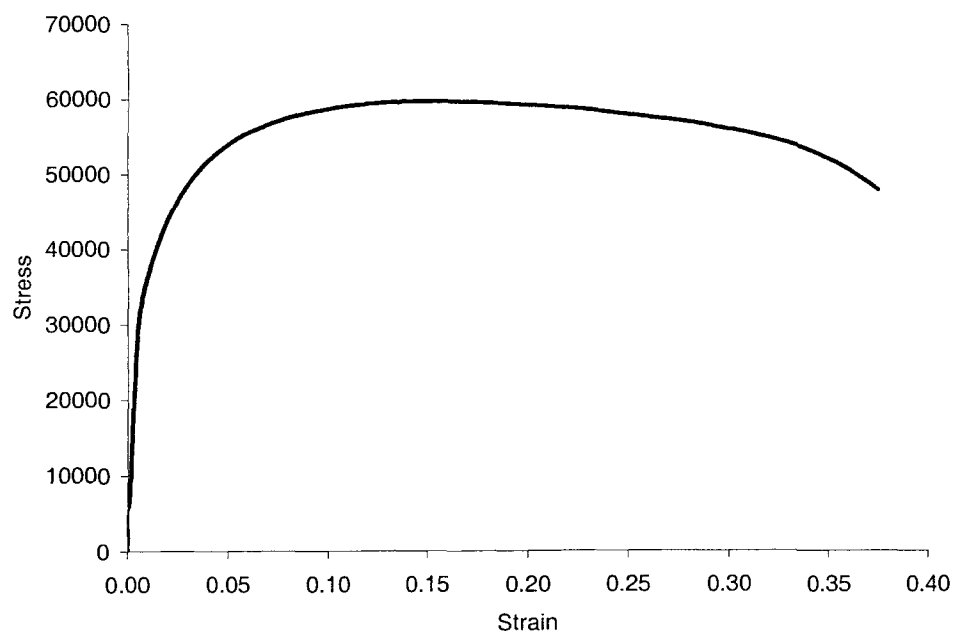
B2. SSR DATA WITHOUT E_{cont} (SMOOTH SPECIMENS)

	Envmnt	Temp (°C)	%El	%RA	σ_f ksi/(Mpa)	TTF (hr)	ϵ_f
106	Air	30	38.0	28.12	63.63	34.22	0.3844
107	Air	30	40.72	30.71	62.47	36.69	0.4059
108	Air	30	39.68	28.55	61.45	35.67	0.3913
120	Air	30	38.18	28.31	63.76	34.63	0.4045
93	Acidic	30	36.18	27.55	62.22	33.80	0.3829
60	Acidic	30	36.52	25.83	62.31	32.84	0.3634
63	Acidic	30	36.07	25.76	61.56	34.82	0.3909
67	Acidic	30	36.80	26.90	62.81	33.54	0.3724
112	Acidic	30	36.23	25.76	61.72	34.97	0.3946
69	Acidic	60	40.23	31.64	56.11	35.37	0.4119
57	Acidic	60	40.82	33.20	56.95	34.95	0.4031
56	Acidic	90	41.41	32.42	49.28	34.68	0.4087
91	Acidic	90	41.67	33.92	48.62	37.16	0.4164
55	SI	30	35.58	24.84	61.80	29.20	0.3304
121	SI	60	37.45	29.56	55.18	34.21	0.3859
109	SI	90	39.47	31.29	59.36	34.30	0.3895

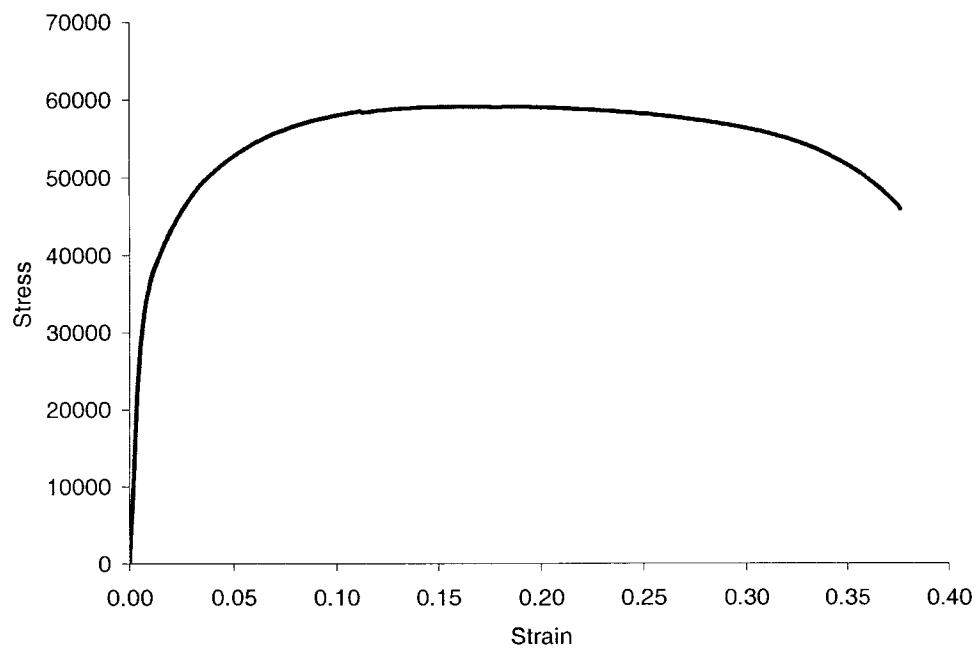
B3.Stress Vs Strain Curves (Smooth Specimens) with E_{cont}



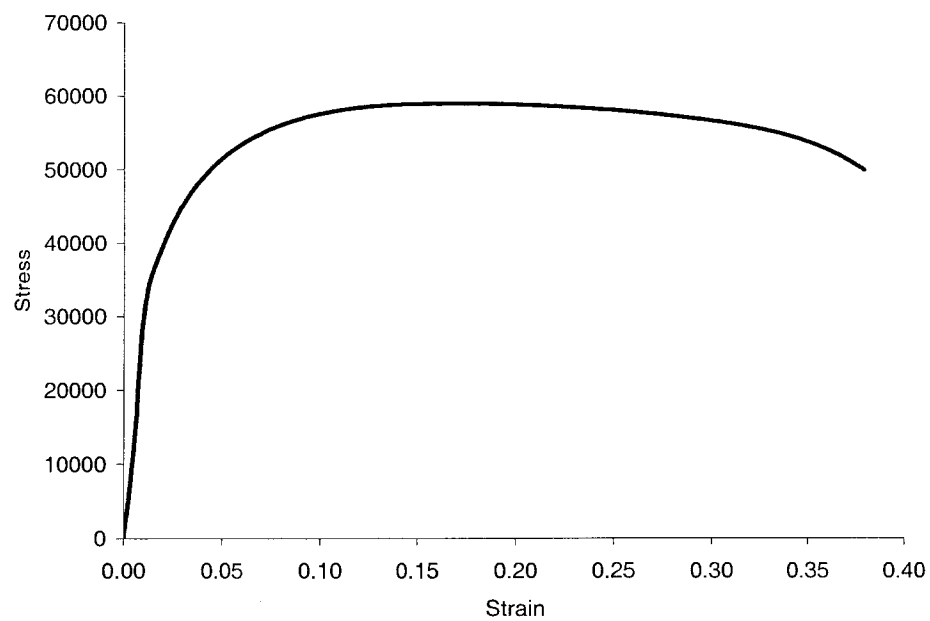
Acidic Environment, Ambient Temperature, $E_{\text{cont}} = -675$ mV (Sample 1)



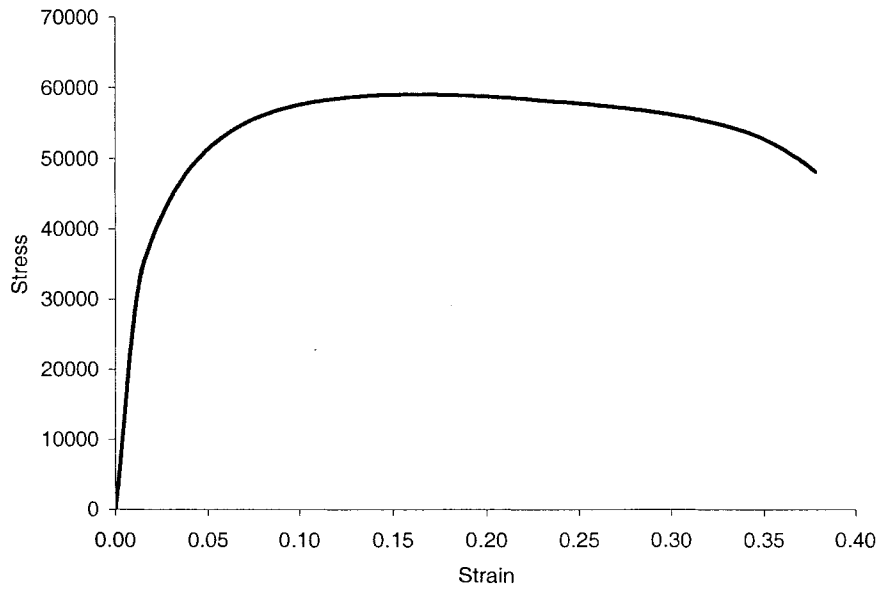
Acidic Environment, Ambient Temperature, $E_{\text{cont}} = -675$ mV (Sample 2)



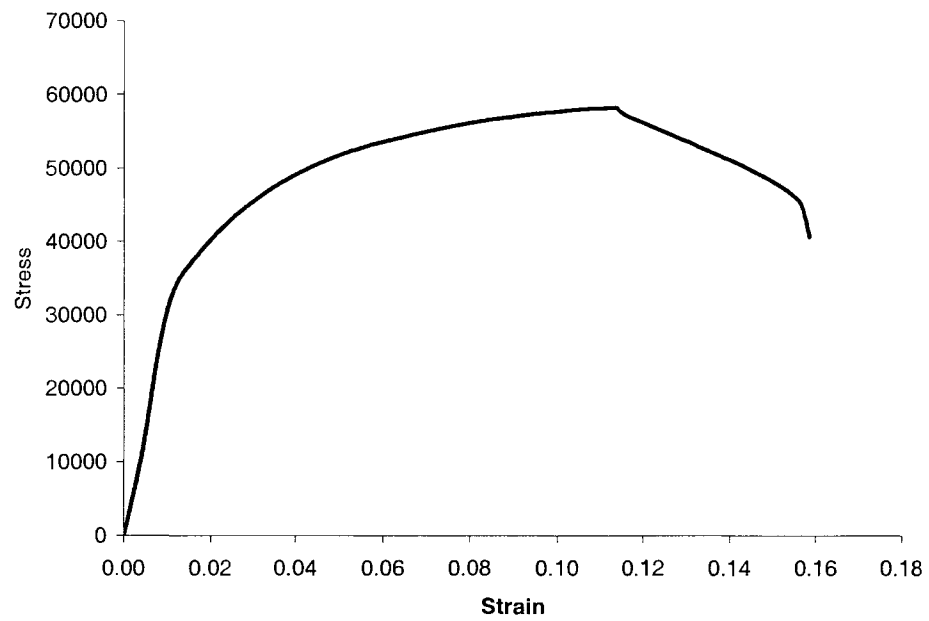
Acidic Environment, Ambient Temperature, $E_{\text{cont}} = -875$ mV (Sample 1)



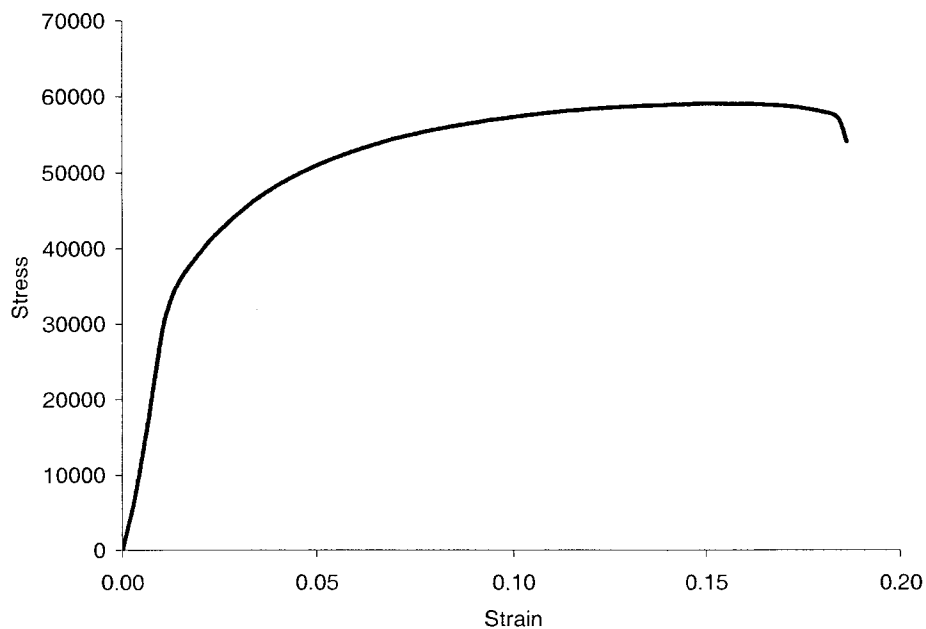
Acidic Environment, Ambient Temperature, $E_{\text{cont}} = -875$ mV (Sample 2)



Acidic Environment, Ambient Temperature, $E_{\text{cont}} = -1000$ mV (Sample 1)



Acidic Environment, Ambient Temperature, $E_{\text{cont}} = +500$ mV (Sample 1)



Acidic Environment, Ambient Temperature, $E_{\text{cont}} = +500 \text{ mV}$ (Sample 2)

B4. SSR DATA WITH E_{cont} (SMOOTH SPECIMENS)

Material	Potential	%EI	%RA	σ_f ksi/(Mpa)	TTF (hr)	e_f
Zr-2-68	-675 mV	35.05	26.98	69.57/(479.69)	34.34	0.3747
Zr-2-101	-675 mV	35.65	26.66	62.67/(432.11)	34.22	0.3832
Zr-2-104	-875 mV	34.73	25.44	61.43/(423.56)	33.03	0.3763
Zr-2-96	-875 mV	34.88	27.09	62.44/(430.52)	33.17	0.3795
Zr-2-65	-1000 mV	33.8	24.69	59.65/(411.29)	33.87	0.3784
Zr-2-114	+500 mV	21.62	16.04	60.5/(417.15)	14.63	0.1584
Zr-2-116	+500 mV	22.05	17.15	60.72/(418.66)	17.16	0.1864

APPENDIX C

UNCERTAINTY AND STATISTICAL ANALYSES

Every experimental result has a level of uncertainty associated with it, unless it is an exact, counted integer, such as the number of trials performed. This uncertainty in the results can be due to the accuracy and precision of the instruments used, human factors, and the environmental condition. Every calculated result also has an uncertainty, related to the uncertainty in the measured data used to calculate it. There are different models available to do uncertainty analysis for experimental results. One such model is discussed in detail in this section. Unlike uncertainty analysis, a statistical analysis helps to interpret the experimental results correctly. A brief overview of the uncertainty and statistical analysis is provided in this section by randomly choosing one of the parameters evaluated in this investigation.

The uncertainty model proposed by Kline and McClintock ⁽³⁶⁾ is chosen in this analysis. The method is based on a careful specification of the uncertainties in the various primary experimental measurements. For example, the maximum load-cell reading of the slow-strain-rate (SSR) unit is 7500 lbs \pm 0.3% lbs.

When the plus or minus notation is used to designate the uncertainty, the person making this designation is stating the degree of accuracy with which he or she believes

the measurement has been made. It is notable that this specification is in itself uncertain because the researcher is naturally uncertain about the accuracy of these measurements.

If a very careful calibration of an instrument has been performed recently, with standards of very high precision, then the experimentalist will be justified in assigning a much lower uncertainty to measurements than if they were performed with a gage or instrument of unknown calibration history. The level of uncertainty is also dependent on the calibration standard. Instruments having high accuracy and operating in controlled environments should have a shorter calibration interval compared to rugged instruments used for everyday purposes.

Most of the instruments in the Materials Performance Laboratory (MPL) were calibrated on a regular basis by Bechtel Nevada using standards with very high precision and traceable to the national standards. Thus, it is expected that the resultant data presented in this thesis would have very low uncertainties. The uncertainties in the results of this investigation are calculated by using the Kline and McClintock Method. The equation used for this method is given below.

$$W_R = \left[\left(\frac{\partial R}{\partial x_1} w_1 \right)^2 + \left(\frac{\partial R}{\partial x_2} w_2 \right)^2 + \cdots + \left(\frac{\partial R}{\partial x_n} w_n \right)^2 \right]^{\frac{1}{2}} \dots\dots\dots (C 1.1)$$

Where, W_R = the uncertainty in the results

R = the given function of the independent variables x_1, x_2, \dots, x_n)

$R = R(x_1, x_2, \dots, x_n)$

w_1, w_2, \dots, w_n = the uncertainty in the independent variables

C.1 Uncertainty Calculation for YS Derived from MTS Results

The results generated from the MTS testing are stress (σ), percentage elongation (%El), and percentage reduction in area (%RA). The stress is based on the load (P) and the initial cross-sectional area (A_i) of the tested specimen. The %El is based on the change in length (Δl) during the testing and the %RA is based on the initial and final cross-sectional areas (A_i and A_f). The magnitude of P was obtained from the load-cell of the MTS unit. However, the values for Δl , A_i , and A_f were calculated based measurements by a caliper. The uncertainties in load-cell and caliper were $\pm 0.03\%$ lbs and ± 0.001 in, respectively, obtained from the calibration. The uncertainty in the initial notched diameter was ± 0.001 , which was provided by the manufacturer and the uncertainty in the final notched diameter was ± 0.001 obtained by using the caliper.

C.1.1 Calculation of Uncertainty in Stress (U_σ)

$$U_\sigma = U_{(P, A_i)}$$

$$U_{A_i} = (U_{D_i})^2$$

$$\text{Uncertainty in load-cell} = \pm 0.03\% \text{ lb}$$

$$\text{Uncertainty in caliper} = \pm 0.001 \text{ in}$$

Sample calculation:

$$\text{For yield stress (YS)} = 53.05 \text{ ksi}$$

$$\text{Uncertainty in load (} U_p \text{)} = 2602.77 * 0.0003$$

$$= \pm 0.781$$

Uncertainty in cross-sectional area (U_{A_i}) for the smooth specimen:

$$\text{Initial Diameter (} D_i \text{)} = 0.25 \text{ in}$$

Uncertainty in diameter (u_D) = ± 0.001 in

$$\text{Area } (A_i) = \frac{\pi D_i^2}{4}$$

$$= 0.049$$

$$\frac{dA_i}{dD_i} = \frac{\pi D_i}{2}$$

$$= 0.393$$

$$\text{Uncertainty in area, } U_{A_i} = \left[\left(\frac{dA_i}{dD_i} \cdot U_{D_i} \right)^2 \right]^{\frac{1}{2}}$$

$$= 0.393 \cdot 0.001$$

$$= \pm 0.000393$$

$$\text{Uncertainty in stress, } U_{\sigma} = \left[\left(\frac{\partial \sigma}{\partial P} \cdot u_P \right)^2 + \left(\frac{\partial \sigma}{\partial A_i} \cdot u_{A_i} \right)^2 \right]^{\frac{1}{2}} \dots\dots\dots (2)$$

$$\sigma = \frac{P}{A_i}$$

$$\frac{\partial \sigma}{\partial P} = \frac{1}{A_i}$$

$$= 20.41$$

$$\frac{\partial \sigma}{\partial A_i} = -\frac{P}{A_i^2}$$

$$= -1081276$$

Now providing all the numerical values in equation C.1.1 obtained from the calculation, it is found that,

$$\begin{aligned}U_{\sigma} &= \left[(20.41 * 0.781)^2 + (-1081276 * 0.000393)^2 \right]^{\frac{1}{2}} \\&= 425.24 \text{ psi} \\&= \pm 0.43 \text{ ksi}\end{aligned}$$

One example of the use of the uncertainty analysis is shown in this section. This can be implemented to all experimental results discussed in this thesis.

Statistical methods are widely used to study the significance of experimental results. For example, a “*t test*” can be used to study if the observed values are coming from a population with a specified mean. These tests gives solid evidence to the conclusions derived from the experimental results. In this section, the time-to-failure (TTF) of SSR experiments conducted in air and acidic solution at ambient temperature are taken and compared if they differ significantly or not. A significant difference implies that there is an effect of the acidic solution on the TTF at ambient temperature under the SSR condition. A minimum of three samples under each treatment is required for this kind of analysis. A “*t test*” is sufficient for analysis of two treatments. But in this analysis, an Analysis of Variance (ANOVA) method is considered because of its simplicity and accuracy. The four replicates of the two treatments are given in Table C.1.

Table C.1. TTF for the Selected Treatments

Sample No	Air	30°C Acidic
1	34.22	33.8
2	36.69	32.84
3	35.67	34.82
4	34.63	33.54

Table C.2. Analysis of the Treatments

	Air	30°C Acidic	
Σx	141.21	135	
n	4	4	
Mean	35.3025	33.75	
Σx^2	4988.7503	4558.2696	
$(\Sigma x)^2$	19940.2641	18225.0000	
Σd^2	3.684275	2.0196	$\Sigma d^2 = \Sigma x^2 - (\Sigma x)^2/n$
σ^2	1.22809167	0.6732	$\Sigma d^2/n-1$
σ	1.10819297	0.82048766	$\sigma = \text{Sqrt}(\sigma^2)$
σ_n	0.55409649	0.41024383	$\sigma_n = \sigma/\text{sqrt}(n)$

The analyses of the treatments are shown in Table C.2. and the completed ANOVA table is shown in Table C.3. An F-ratio of the mean square for treatments and mean square for residual gives a value of 5.07. For an α value of 0.05, the table value is 10.1. As the calculated F value is less than the table value, the difference between the two treatments is insignificant at a producer's risk of 0.05.

Table C.3 ANOVA Table

Source of Variance	Sum of Squares (S of S)	Degrees of Freedom (df)	Mean Square = Sof S/df
Between Treatments	4.8205125	$u-1 = 1$	4.8205125
Residual	5.7039	$u(v-1) = 6$	0.950645833
Total	10.5243875	$(uv)-1=7$	

This result implies that there is no significant difference between the TTF of tests conducted in air and 30°C acidic solution. So, we can safely conclude that there is no effect of acidic solution at ambient temperature on the TTF under the SSR condition. Similar type of analysis could not be conducted for the other experimental results, as there were only two replicates for each type of experiment.

BIBLIOGRAPHY

1. Nuclear Regulatory Commission Website,
<http://www.nrc.gov/waste/spent-fuel-storage.html>
2. Nuclear Regulatory Commission Website,
<http://www.nrc.gov/reading-rm/doc-collections/nuregs/staff/sr1437/v1/part06.html>
3. National Spent Nuclear Fuel Program Website,
<http://nsnfp.inel.gov/whatis6.asp>
4. Technical Information Supporting Site Recommendation Consideration, "Yucca Mountain Science and Engineering Report, Rev 1. DOE/RW-0539-1" (2002).
5. C. Pestcatore et al., "Zircaloy Fuel Performance under Spent Fuel Disposal Conditions, BNL-52235, DOE/OSTI-4500-R75, WMEM-ZRC Rev. 4/90", Progress Report for May 1-October 31, 1989, Brookhaven National Laboratory (1990).
6. B.G.Parfenov, V.V.Gerasimov and G.I.Vendiktova., Corrosion of Zirconium and Zirconium Alloys, pp. 1-3 (1969).
7. Delayed Hydride Cracking in Zirconium alloys in pressure-tube nuclear reactors International Atomic Energy Agency-TECDOC 1410, Final Report of Coordinated Research Project, (1998-2002).
8. L. A. Simpson and M. P. Puls., Effect of Stress, Temperature and Hydrogen content on hydride-induced crack growth in Zr-2.5 % Nb, Metall Trans. A, 10A, pp. 1093 (1979).
9. H.M. Chung., Corrosion and Hydride-Induced Degradation of spent Fuel Cladding under Repository Conditions, Energy Technology Division, Argonne National Laboratory, (1999).
10. D. E. Thomas, F. Forscher, "*Properties of Zircaloy-2.*" WESTINGHOUSE ELECTRIC CORP PITTSBURGH PA.
11. Yucca Mountain Science and Engineering Report Rev 1, DOE/RW-0539-1
12. S. W Sharkawy, F.H Hammad, A.A Abou-Zahara, k. Videm "Influence of some factors on the susceptibility of Zircaloy-2 tubes to iodine stress corrosion cracking." *Journal of Nuclear Materials*, 165, pp. 184-192 (1989)

13. Corrosion doctors, corrosion resource, <http://www.corrosionsource.com>
14. Te-Lin Yau, Teledyne Wah Chang Albany., Stress-Corrosion Cracking of Zirconium Alloys.
15. Wah Chang Certified Test Reports for Chemical Composition of Zircaloy-2 (Heat # 242831), September 2001.
16. Baldev Raj, "Materials in Nuclear Industry", Training School Lectures on Metallurgy and Material Science, Indira Gandhi Centre for Atomic Research.
17. Wah Chang Certified Test Reports for Mechanical Properties of Zircaloy-2 (Heat # 242831), September 2001.
18. DOE Fundamentals handbook Material Science, Vol2 of 2, pp. 56-58 (1993)
19. Webster, R.T., Zirconium and hafnium. Metal Handbook tenth edition 2, pp. 661-669, (1990)
20. ASTM Designation E 8-04, "Standard Test Methods for Tension Testing of Metallic Materials," American Society for Testing and Materials (ASTM) International.
21. March, J.L., Ruprecht, W. J., and Reed, George, "Machining of Notched Tension Specimens," ASTM Bulletin, ASTBA, Am.Soc.Testing Mats., No.244, pp.52-55 (1960)
22. ASTM Designation G 5-94 (1999) e1, "Standard Reference Test Method for Making Potentiostatic and Potentiodynamic Anodic Polarization Measurements," American Society for Testing and Materials (ASTM) International.
23. Subhas Pothana, "Evaluation of Cracking and Localized Corrosion Behavior of Cladding Materials," M.S. Thesis, Dept. of Mechanical Engineering, University of Nevada, Las Vegas, December 2003.
24. Heidi Aquino, "Cracking of Zirconium Alloys at Constant Load with and without Applied Potentials," M.S. Thesis, Dept. of Mechanical Engineering, University of Nevada, Las Vegas, December 2003.
25. Cortest, Incorporated Website (www.cortest.com)
26. A.K. Roy, et al., "Environment-Assisted-Cracking of Cladding Materials under Different Loading Conditions", IHLRWM, Las Vegas, NV, Mar-April 2003.
27. ASTM Designation G 129-00, "Standard Practice for Slow Strain Rate Testing to Evaluate the Susceptibility of Metallic Materials to Environmentally Assisted Cracking," American Society for Testing and Materials (ASTM) International.

28. Slow-Strain-Rate Testing, Corrosion Source Website
<http://www.corrosionsource.com/handbook/testing/ssrt.htm>
29. A. K. Roy, et al., "Effect of Controlled Potential on SCC of Nuclear Waste Package Container Materials," *Proceedings of NACE Corrosion 2000*, Paper No. 00188, Orlando, FL (2000)
30. A.K. Roy, et al., "Stress Corrosion Cracking of Ni-Base and Ti Alloys Under Controlled Potential," 7th International Conference on Nuclear Engineering, Paper No. ICONE-7048, Tokyo, Japan, April 19-23, 1999
31. A.K. Roy, et al., "Cracking of Titanium Alloys under Cathodic Applied Potential," *Micron*, Elsevier Science, Vol 32, No. 2, pp. 211-218, Feb 2001.
32. Polarization Behavior, Corrosion Doctors Website
(<http://www.corrosion-doctors.org/Kinetics/Polarization.htm>)
33. ASM Handbook, "Metallography and Microstructures," Vol 9, 9th Edition, pp. 501, American Society for Metals (2000).
34. ASM Handbook, "Properties and Selection: Non-Ferrous Alloys and Special Purpose Materials," Vol 2, 10th Edition, pp. 667, American Society for Metals (2000).
35. A.K Roy, D. L Fleming, B.Y Lum, "Localized Corrosion Behavior of Candidate Nuclear waste Package Container Materials", *Material Performance*, NACE International, pp. 54-58. March 1998
36. Jack P. Holman, "Experimental Methods for Engineers," McGraw-Hill Book Company, 4th Edition, pp. 50

VITA

Graduate College
University of Nevada, Las Vegas

Unnikrishnan Valliyil

Local Address:

4223 Grove Circle, Apt # 3
Las Vegas, NV 89119

Permanent Address:

2988 E. Reno Avenue
Las Vegas, NV 89120

Degree:

Bachelor of Engineering, Production Engineering, 2001
Bharathiar University, Coimbatore, India

Special Honors and Awards:

- Secured I Rank in the University Examination during Undergraduate(B.E).
- Secured the III prize for presentation in ANS Student Competition, Ohio 2005, Material Science and Technology Stream
- ASQ Certified Quality Engineer (CQE)

Selected Publications:

- Ajit K. Roy, Unnikrishnan Valliyil, et al., "Corrosion behavior of Zirconium Alloys With and Without Applied Potential," *Journal of ASTM International*.
- Ajit K. Roy, Unnikrishnan Valliyil, et al., "Stress Corrosion Cracking of Cladding Materials," *Proceedings of TMS Conference, San Francisco 2005*.
- Unnikrishnan Valliyil, "Cracking of Zircaloy-2 Under Cathodic Applied Potential," *Proceedings of ANS Student Conference, OH 2005*.
- Ajit K. Roy, Unnikrishnan Valliyil, et al., "Cracking of Zirconium Alloys Under Controlled Cathodic Potential," *Proceedings of SAMPE Conference, Long Beach, (CA) 2005*.